

Formation of Long-Lived Summertime Mesoscale Vortices over Central East China: Semi-Idealized Simulations Based on a 14-Year Vortex Statistic

SHEN-MING FU

*International Center for Climate and Environment Sciences, Institute of Atmospheric Physics, Chinese Academy of Sciences,
Beijing, China*

JIAN-HUA SUN

*Laboratory of Cloud-Precipitation Physics and Severe Storms, Institute of Atmospheric Physics, Chinese Academy of Sciences,
and State Key Laboratory of Severe Weather, Chinese Academy of Meteorological Sciences, Beijing, China*

YA-LI LUO

State Key Laboratory of Severe Weather, Chinese Academy of Meteorological Sciences, Beijing, China

YUAN-CHUN ZHANG

*Laboratory of Cloud-Precipitation Physics and Severe Storms, Institute of Atmospheric Physics, Chinese Academy of Sciences,
Beijing, China*

(Manuscript received 15 November 2016, in final form 6 September 2017)

ABSTRACT

Regions around Dabie Mountain (DBM) in the Yangtze River basin (YRB) are the source of a mesoscale vortex: the Dabie vortex (DBV). Based on a 14-yr statistical study, 11 long-lived heavy-rain-producing DBVs were composed for convection-permitting semi-idealized simulations. A control simulation, initialized 12 h before the composite vortex formation, successfully reproduced a DBV, with all the salient characteristics of the 11 events. Sensitivity experiments were designed to understand the impacts of large-scale environmental conditions, regional topography, and latent heating on DBV formation. The main results were as follows: (i) Supposition of a 500-hPa shortwave trough with an east-west-oriented lower-level transversal trough around the DBM is crucial for the formation of vortices. A nocturnal lower-level jet on the southern side of the transversal trough accelerates DBV formation by enhancing convergence, triggering/sustaining convection, and producing cyclonic vorticity. (ii) During the simulation period, the topography east of the second-step mountain ranges, including the DBM, significantly affects nearby precipitation and convective activity, whereas this is not crucial for DBV formation. (iii) Latent heating is not required for generating DBVs, but it enhances the intensity, longevity, and eastward progression of these vortices along the shear line associated with the transversal trough. (iv) The vorticity budget suggests the convergence-related (horizontal) shrinking and vertical transport dominate the cyclonic-vorticity increase associated with DBVs, whereas tilting and horizontal transport mainly act in the opposite manner.

1. Introduction

Statistical and climatological studies (Yang et al. 2010; Zhang et al. 2015) have shown that regions around Dabie Mountain (DBM) over the Yangtze River basin (YRB) in central east China (Fig. 1a) are an important vortex source. The vortices originate around DBM, are

typically of the meso- α scale (Orlanski 1975), and have been named Dabie vortices (DBVs) (Fu et al. 2016; Zhang et al. 2015). This type of vortex is particularly noteworthy, because (i) it has a high frequency of occurrence [with a mean monthly frequency of occurrence of ~ 12.2 (Fu et al. 2016)], (ii) it is extremely likely to trigger precipitation [$\sim 92\%$ of DBVs induce rainfall events (Fu et al. 2016)], and (iii) long-lived DBVs can last for several days and continuously trigger heavy

Corresponding author: Shen-Ming Fu, fum@mail.iap.ac.cn

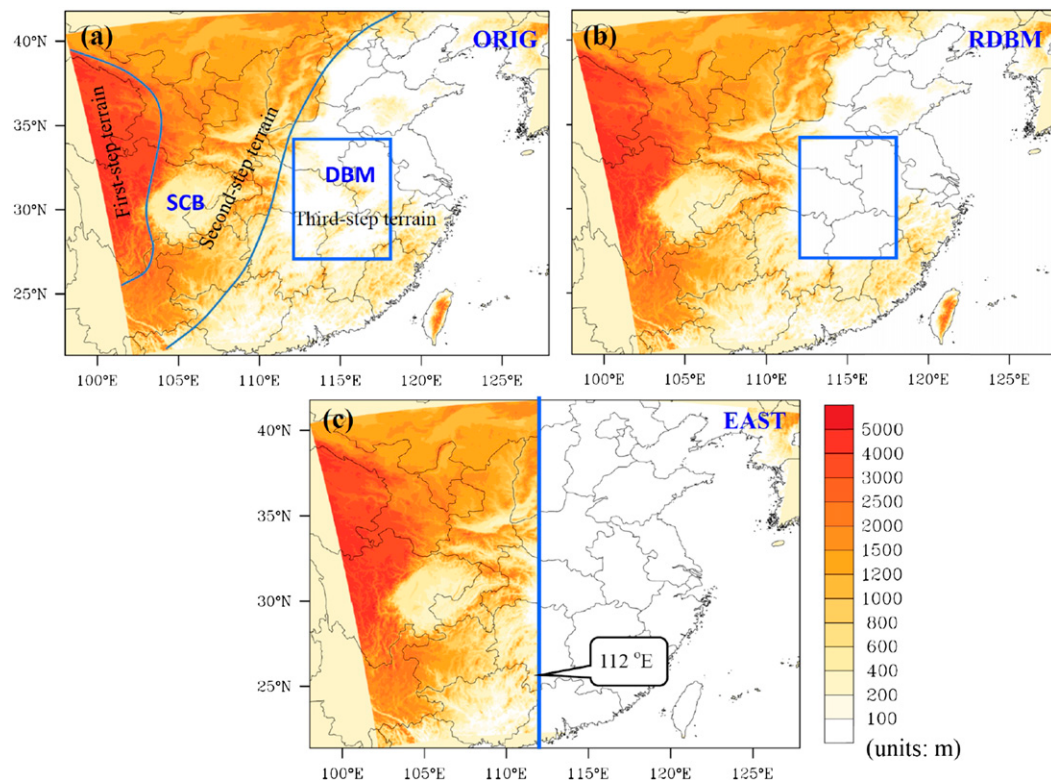


FIG. 1. Terrain height (shading) used for the semi-idealized simulations (d03). The blue rectangle marks the source region of the DBV.

rainfall events (Table 1), resulting in severe flood disasters over the YRB (Fu et al. 2013; Sun et al. 2010). However, it is not known why the region around DBM is the source of DBVs, nor whether the topographic features around DBM (Fig. 1a) provide the decisive conditions for the formation of this vortex. Moreover, although it is closely related to precipitation, how latent heating affects the formation of DBVs is still unclear. Thus, the primary objective of this study was to address these three issues.

Owing to heavy rainfall events, flooding and water-logging disasters often occur over the YRB in central east China—for example, the 1931 YRB flood (Tao 1980) and the 1998 YRB flood (Zhao et al. 2004). The mesoscale vortices account for a considerable proportion of the heavy precipitation in this region (Ding 1993; Tao 1980; Zhao et al. 2004). Previous studies have mainly focused on two types of vortices: that is, the southwest vortex (SWV), which originates from the Sichuan basin (SCB; Fig. 1a) (Lu 1986), and the DBV that forms around DBM. Both types of vortex appear frequently in summer (Fu et al. 2016). It has been suggested that the topography of the Sichuan basin east of the Tibetan Plateau provides advantageous conditions for SWV formation through frictional convergence (Lu

1986). This might be a reason why the regions around the Sichuan basin are the source of SWVs. For the DBVs, why they frequently form around DBM is still a mystery. Some studies have speculated that the topography around DBM contributes to DBV formation through orographic lifting (Hu and Pan 1996; Zhou and Li 2010). However, whether the topography around DBM is a decisive factor in DBV formation remains unclear. Many DBVs are associated with a midlevel

TABLE 1. Initiation time, life span, and maximum 6-hourly observed precipitation of the long-lived DBVs.

No.	Initiation time	Life span (h)	Maximum precipitation (mm)
1	1800 UTC 13 Jul 2001	72	93
2	1800 UTC 09 Aug 2001	108	23
3	1200 UTC 18 Jun 2004	72	24
4	0600 UTC 10 Jul 2004	78	57
5	0000 UTC 22 Aug 2005	84	51
6	0000 UTC 27 Jun 2007	78	76
7	0000 UTC 09 Jul 2008	96	53
8	0000 UTC 14 Aug 2008	66	56
9	0600 UTC 16 Aug 2008	72	87
10	0000 UTC 30 Aug 2008	78	88
11	1200 UTC 06 Jun 2013	120	102

shortwave trough (Hu and Pan 1996; Zhang et al. 2015) and a lower-level jet (LLJ) (Gao and Xu 2001; Sun et al. 2010; Zhou and Li 2010), which provides favorable conditions (e.g., ascent and moisture transport) for heavy precipitation. In related weather analyses, latent heating is regarded as a key factor in the formation (Gao and Xu 2001; Sun et al. 2010) and longevity of DBVs (Fu et al. 2016). However, no other studies have confirmed this or have shown how latent heating affects DBVs. Similar to the mesoscale convective vortices (MCVs), which are known to form within the trailing stratiform region of MCSs (Bartels and Maddox 1991; Davis et al. 2004; Galarneau et al. 2009), a cold pool is also often found at lower levels of the DBVs. Previous studies (Clark et al. 2010; Kirk 2003; Knievel and Johnson 2003; Olsson and Cotton 1997; Zhang 1992) have shown that a cold pool can affect MCV evolution through its interaction with convection and convergence (e.g., via tilting and stretching related vorticity production). However, for DBVs, how the cold pool influences their formation still needs to be answered.

The remainder of this paper is organized as follows. Section 2 describes the dataset, model configuration, semi-idealized¹ simulation design, and vorticity budget method. Section 3 explains the simulation verification, synoptic-scale background conditions for vortex formation, and the evolution of convective activity and kinematic features during the formation stage (the period from no DBV to DBV formation; i.e., from $t = 0$ to $t = 11$ h). Section 4 presents the vortex-averaged features and vorticity budget. Sensitivity experiments regarding the latent heating/cooling and topography are discussed in section 5. Section 6 provides a possible cause of the formation of DBVs. Finally, a conclusion and discussion is given in section 7.

2. Data, setup and design of semi-idealized simulations, and methodology

a. Data and configuration of the model

Multiscale processes leading to the formation of DBVs were simulated using a one-way triple-nested (27, 9, and 3 km), convection-permitting version of the Advanced Research WRF (Skamarock et al. 2008). The domains (d01, d02, d03)² consisted of 301×241 , 421×361 , and 811×721 grid points, respectively (not shown), with 30 vertical levels in the vertical and model top at 50 hPa.

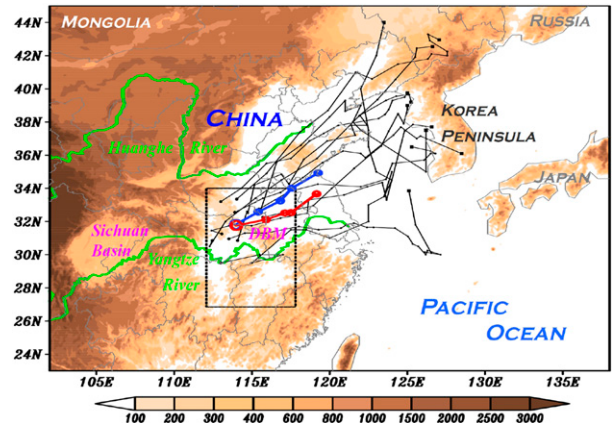


FIG. 2. Tracks of the 11 long-lived PL-DBVs (thin black solid lines), the averaged moving track [thick blue line with open circles (6-h interval)], where the large blue open circle represents the location of initiation, and the simulated moving track in the ORIG run [thick red line with open circles (6-h interval)], where the large red open circle represents the location of formation]. The black dashed rectangle marks the DBV source region.

The WRF single-moment 6-class microphysics scheme (WSM6) (Hong and Lim 2006), the Yonsei University (YSU) planetary boundary layer scheme (Noh et al. 2001), and the Noah land surface model (Chen and Dudhia 2001) were used in all three domains. The Kain–Fritsch cumulus parameterization (Kain 2004) was only used in d01 and was turned off in d02 and d03. A comparative test showed that the simulation results of d03 were not sensitive to the use of a cumulus scheme in d02. The National Centers for Environmental Prediction (NCEP) Climate Forecast System Reanalysis (CFSR) $0.5^\circ \times 0.5^\circ$ data (Saha et al. 2010) were used as the initial and boundary conditions for the semi-idealized simulations. Rain gauge-based 6-h accumulated precipitation data from the China Meteorological Administration were used to evaluate the simulated precipitation associated with DBVs.

b. Design of semi-idealized simulations

Fu et al. (2016) conducted a 14-yr (2000–13) statistical analysis of summertime DBVs using the $0.5^\circ \times 0.5^\circ$ NCEP CFSR data. They classified DBVs into four types according to whether obvious precipitation occurred and whether a closed surface low center appeared within a 6-h period before the formation of a vortex. These four types were referred to as precipitation and surface low (PL), precipitation only (PN), surface low only (NL), and no precipitation and no surface low (NN). Among these four vortex types, PL type had the strongest intensity, largest three-dimensional size, longest lifetime, and heaviest precipitation.

¹A semi-idealized simulation means an idealized simulation based on real situations.

²In this study, all analyses used the output from d03, except for the large-scale features, which were based on the output from d01.

TABLE 2. List of sensitivity experiments and associated model configurations.

Expt	Objectives	Latent heating/cooling options	Terrain features
ORIG	Original semi-idealized run	Turn on both the latent heating and cooling	Original model terrain (Fig. 1a)
NOEC	Sensitivity to zeroing only the evaporative cooling	Turn off the evaporative cooling within the cold pool region (29° – 35° N, 110° – 118° E)	As in ORIG
NOLH	Sensitivity to zeroing only the latent heating	Turn off the latent heating within the cold pool region (29° – 35° N, 110° – 118° E)	As in ORIG
FAKE	Sensitivity to latent heating/cooling	Turn off both the latent heating and cooling	As in ORIG
RDBM	Sensitivity to the topography around DBM	As in ORIG	Removing the topography around DBM (Fig. 1b)
EAST	Sensitivity to the topography to the east of 112° E over China	As in ORIG	Removing the topography to the east of 112° E (Fig. 1c)

Using 42 h as the threshold for the longevity of a DBV, Fu et al. (2016) selected 11 long-lived PL-DBVs from all 43 PL-DBV events. These long-lived events all induced torrential precipitation during their lifetime (Table 1) and mainly moved northeastward (Fig. 2). Previous case studies (Gao and Xu 2001; Sun et al. 2010; Zhou and Li 2010) have suggested some common characteristics among DBVs during their formation stage, which could explain why the regions around DBM act as a source for this type of vortex. Therefore, the initial and boundary conditions for the semi-idealized simulations were determined by the composite of these long-lived events. To mainly focus on the formation stage, the semi-idealized simulations ran for 36 h (i.e., 12 h before the formation of a vortex and 24 h after its initiation).

The formation time of each DBV was defined as $V_n(0)$, where n represents the number of vortices, and V denotes a sample variable. The time series $V_n(-2)$, $V_n(-1)$, $V_n(0)$, $V_n(1)$, $V_n(2)$, $V_n(3)$, and $V_n(4)$, with an interval of 6 h, represents the period from 12 h before the initiation of a vortex n to 24 h after its formation. For the 11 long-lived PL-DBVs, the corresponding times were composited (equally weighted) based on the Euler viewpoint, which results an ideal 36-h time series. This ideal time series with a 6-h interval was used as the initial and boundary conditions for the simulations in Table 2: original (ORIG), no evaporative cooling (NOEC), no latent heating (NOLH), fake dry (FAKE), removing DBM (RDBM), and removing topography east of 112° E (EAST). The start time of the simulation was the temporal average (only the integer portion) of the start times of all 11 events (Table 1). For this study, $t = 0$ h corresponded to 0600 UTC or 1400 Beijing standard time (BST).

c. Vorticity budget method

The vorticity budget has been widely used to understand the evolutionary mechanisms of mesoscale vortices (Davis and Galarneau 2009; Fu et al. 2013, 2015b; Olsson and Cotton 1997; Sun et al. 2010). In this study, the vorticity budget equation from Kirk (2003) was used to determine the main factors during the formation of DBVs:

$$\frac{\partial \zeta}{\partial t} = \underbrace{-\mathbf{V}_h \cdot \nabla_h \zeta}_{\text{HAV}} - \underbrace{\omega \frac{\partial \zeta}{\partial p}}_{\text{VAV}} + \underbrace{\mathbf{k} \cdot \left(\frac{\partial \mathbf{V}_h}{\partial p} \times \nabla_h \omega \right)}_{\text{TIL}} - \underbrace{\beta v}_{\text{AP}} - \underbrace{(\zeta + f) \nabla_h \cdot \mathbf{V}_h}_{\text{STR}} + \text{RES}, \quad (1)$$

where ζ is the relative vorticity; $\mathbf{V}_h = u\mathbf{i} + v\mathbf{j}$ is the horizontal wind vector; \mathbf{i} , \mathbf{j} , and \mathbf{k} are the unit vectors pointing to the east, north, and zenith, respectively; $\nabla_h = (\partial/\partial x)\mathbf{i} + (\partial/\partial y)\mathbf{j}$ is the horizontal gradient operator;³ f is the Coriolis parameter; p is the pressure; $\omega = dp/dt$; and $\beta = \partial f / \partial y$. The terms HAV and VAV represent the horizontal and vertical advection of vorticity, respectively; TIL is the tilting effect; AP represents the planetary vorticity advection, STR is the stretching effect, and RES is the residual effect (including the friction). The total effect (TOT) is defined as $\text{TOT} = \text{HAV} + \text{VAV} + \text{TIL} + \text{AP} + \text{STR}$, which does not include friction-related effects.

According to Green's theorem, the surface integral of vorticity over a region equals the velocity circulation along its boundary line. This means that a vortex

³To guarantee second-order accuracy, all gradient terms were calculated using the centered difference form.

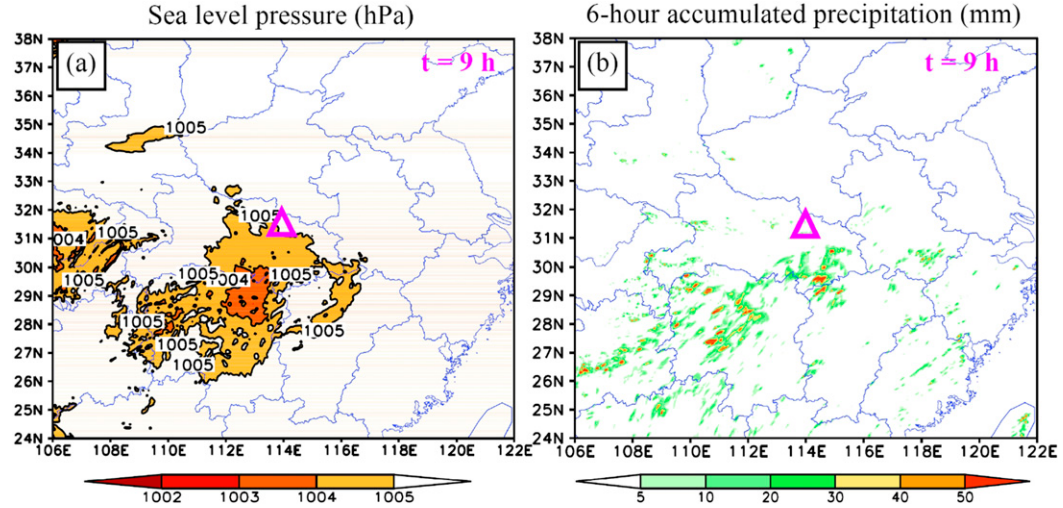


FIG. 3. (a) The ORIG-run-simulated sea level pressure (hPa) before the initiation of the DBV. (b) The ORIG-run-simulated 6-h accumulated precipitation (mm) at the same time. The purple triangle marks the initial location of the DBV.

integral/average of vorticity is an effective measurement for a vortex as a whole. The vortex-averaged vorticity budget and other key features are discussed in detail in section 4.

3. Overview of the DBV formation stage

a. Verification of the ORIG run

The ORIG run (Table 2) was used to analyze the formation of DBVs. Following the definition of Fu et al. (2016), the formation of a DBV was defined only when a meso- α -scale (200–2000 km) vortex structure appeared [i.e., a meso- α -scale closed vortex center (diameter larger than 200 km and smaller than 2000 km) in the stream field coupled with a significant positive vorticity center ($\geq 10^{-4} \text{ s}^{-1}$) (Fu et al. 2015a)]. Because the mean central level of DBVs is ~ 850 hPa (Fu et al. 2016), this level was used as the typical level for analysis. As Fig. 2 shows, although the simulated DBV formed 1 h earlier (at $t = 11$ h; i.e., the model had integrated for 11 h) than the composited DBV, the initiation location of the ORIG-run DBV was very close to that of the composited DBV. The maximum distance between each DBV event and the simulated DBV was ~ 230 km. Before formation of the simulated vortex, a closed surface low center and obvious precipitation appeared around this vortex (Fig. 3). This means the ORIG-run DBV satisfied the criteria for a PL-type DBV (Fu et al. 2016).

As Fig. 2 shows, although the moving track of the simulated DBV differed from that of the composited vortex, both vortices moved northeastward, as did the tracks of most of the 11 long-lived PL-DBVs. Moreover, as the simulated DBV moved northeastward

it increased in size and cyclonic vorticity intensified (Fig. 4). This is consistent with the main evolutionary trends of these 11 long-lived events (Fu et al. 2016). The ORIG run reproduced the main features of the 11 long-lived PL-DBVs reasonably and was, therefore, considered to be representative of this type of vortex.

b. Synoptic-scale background conditions in the ORIG run

During the formation stage, a 200-hPa lee trough was maintained east of the Tibetan Plateau (Fig. 5a). An upper-level jet (ULJ) appeared⁴ ahead of the base of the 200-hPa trough. The formation location of the DBV was around the right entrance region of this ULJ, where its associated secondary circulation contributed to the development of ascending motions (facilitated latent heating and vertical vorticity transport) and lower-level convergence (enhanced production of cyclonic vorticity through stretching) (Holton 2004), with both favoring vortex formation.

In the middle troposphere, a 500-hPa shortwave trough was maintained on the lee side of the second-step terrain⁵ (Fig. 5b). The subtropical high maintained its strength over the northwestern Pacific,

⁴ In this study, following the definitions of Rose et al. (2004) and Clark et al. (2009), 25 m s^{-1} was used as the threshold of a ULJ.

⁵ As the dark blue solid lines in Fig. 1a show, the second-step terrain in China usually refers to the high mountain ranges from the Da Xingan Mountains over northeast China to the Yungui Plateau over southwest China.

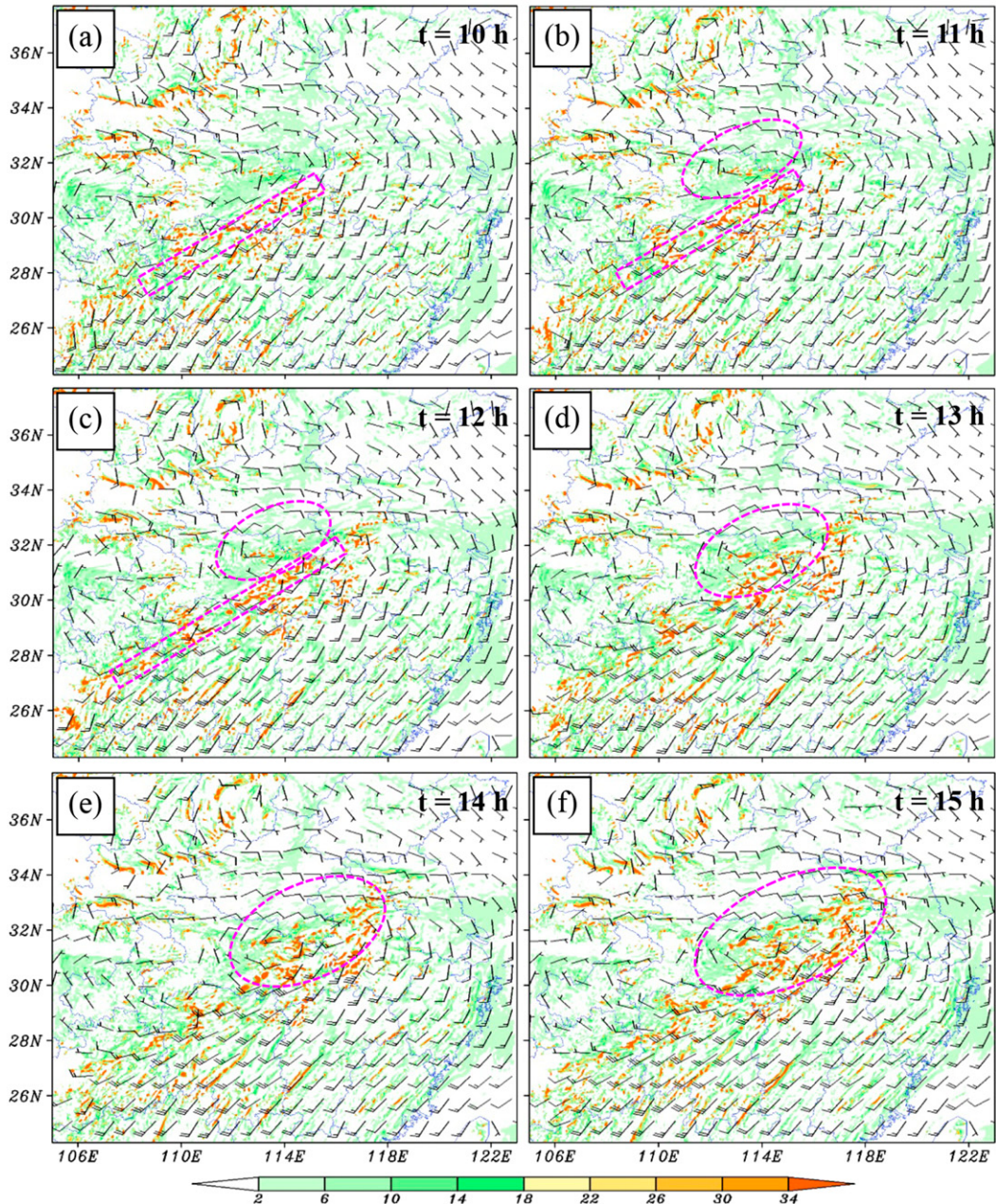


FIG. 4. Evolution of the DBV in the ORIG run. The wind barb stands for the wind at 850 hPa (a full bar represents 5 m s^{-1}), the shading represents vorticity (10^{-5} s^{-1}), the purple dashed ellipses highlight the vortex, and the tilted purple dashed box marks the southwest–northeast cyclonic and convergent line.

which might have favored the quasi-stationary behavior of the 500-hPa trough. Warm advection dominated the regions around DBM. As the wind ahead of the 500-hPa trough base intensified, warm advection was enhanced. This promoted ascending motions through quasigeostrophic forcing (Holton 2004) and favored a decrease in pressure at lower levels (Markowski and Richardson 2010), both of which contributed to the formation of a DBV.

In the lower troposphere, a quasi-stationary transversal trough⁶ persisted east of the Sichuan basin (Fig. 6). Compared to a front, the transversal trough was much wider in range, but had a much weaker temperature gradient (Tao 1980). Because the isothermal

⁶A transversal trough is a synoptic-scale low pressure trough, with an approximate east–west-oriented trough line (Tao 1980).

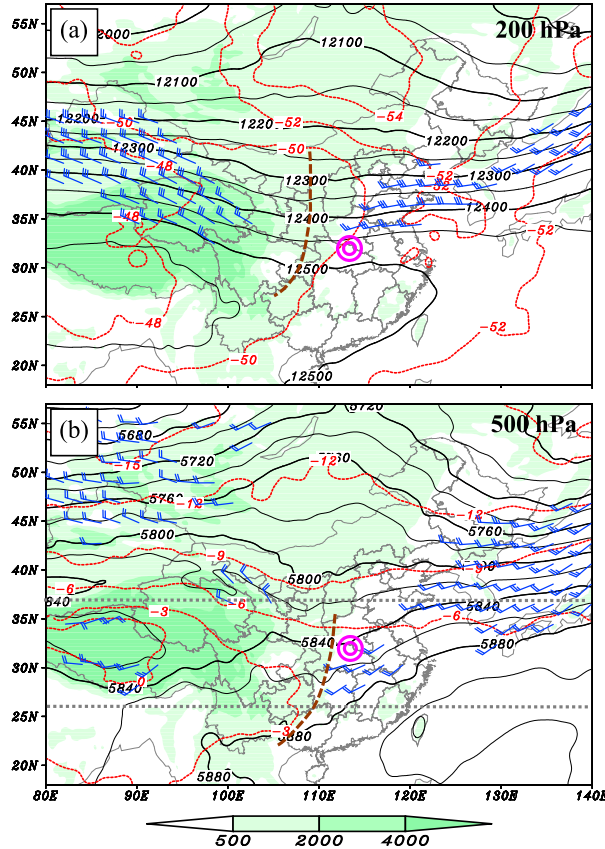


FIG. 5. (a) The 200-hPa geopotential height (black solid lines; gpm), temperature (red dotted lines; °C), and wind speeds $>25 \text{ m s}^{-1}$ (a full bar represents 10 m s^{-1}) at $t = 9 \text{ h}$, in the ORIG run. (b) The 500-hPa geopotential height (black solid lines; gpm), temperature (red dotted lines; °C), and wind speed $>9 \text{ m s}^{-1}$ (a full bar represents 5 m s^{-1}) at $t = 9 \text{ h}$, in the ORIG run. The green shading is the terrain height (m), the purple concentric circle marks the formation location of the DBV, the brown dashed lines are trough lines, and the gray dotted lines show the range for calculating the meridional mean of the shortwave trough (see Fig. 19c).

lines were nearly perpendicular to the transversal trough, warm advection dominated this region, which contributed to the pressure lowering and an enhancement of ascending motions. An LLJ⁷ intensified rapidly on the southern side of the transversal trough. This was a nocturnal LLJ, with its center located around 850 hPa. This LLJ had significant vertical shear (not shown) and featured a significant diurnal variation. According to Van de Wiel et al. (2010) and He et al. (2016), the diurnal variation was a key feature for a nocturnal LLJ. Its

maximum intensity appeared at $\sim 0600 \text{ BST}$, whereas the minimum intensity appeared at $\sim 1700 \text{ BST}$. The intensification of this LLJ from $t = 3$ (1700 BST) to 11 h resulted in stronger warm advection and more intense convergence around the initiation location of the DBV, both of which favored the formation of a vortex.

c. Evolution of convective activity in the ORIG run

An echo with a composite reflectivity $<35 \text{ dBZ}$ appeared around DBM at $t = 3 \text{ h}$ (Fig. 7a). This homogeneous echo was mainly located ahead of the 500-hPa shortwave trough base (Fig. 5a), with its top mainly below 7.5 km and a maximum precipitation rate of $\sim 1 \text{ mm h}^{-1}$ (not shown). All these features indicate this was a stratiform echo, which was triggered by the synoptic-scale lifting of a thick moist layer (not shown). Owing to the evaporative cooling of falling precipitation, a cold pool stretching along the stratiform echo (Fig. 7a) mainly persisted below 825 hPa. Thermodynamically, the cold pool reduced the rate of pressure lowering at the lower levels (Markowski and Richardson 2010) and suppressed local convection through the cooling effect (Schumacher 2009).

During the formation stage, intense convection cells were generated continuously southwest and south of the stratiform echo (Fig. 7). These newborn convective activity was closely related to a southwest–northeast stretching, lower-level convergence and cyclonic line (Figs. 4a,b), which was mainly located along the cold pool's southern boundary (Fig. 7). From $t = 6$ to 12 h , the southwesterly wind ahead of the base of the 500-hPa trough accelerated gradually (not shown), which favored the northeastward displacement of the stratiform echo (Figs. 7b–d). Meanwhile, the LLJ on the southern side of the transversal trough strengthened and enlarged northeastward (Figs. 7b–d). Correspondingly, new convection cells intensified, moved northward, and merged with the stratiform echo, which enhanced the precipitation. As a result of the enhanced evaporative cooling (not shown), the cold pool intensified and enlarged in the southwest–northeast direction. New convective echoes were primarily located around the southern side of this cold pool (Figs. 7b–d) where convergence was strong. In contrast, the cold pool's northern side had very few new convective cells, mainly because of the inhibition of convective activity by the cooling effect and the lack of an energy supply (Schumacher 2009). Intensification of the cold pool caused an increase in height/pressure at lower levels (Fig. 8). In response to the pressure rising, a northerly isallobaric wind appeared (Ralph et al. 1998) around the southern boundary of the DBV (Fig. 8). This reduced the meridional component of the southwesterly wind

⁷ LLJs over the United States differ significantly from those over China; Wei et al. (2014) developed an adaptive criterion for LLJs over China. This criterion has a lower limit of wind speed of 6 m s^{-1} . Therefore, 6 m s^{-1} was also used as the lower limit for an LLJ in the present study.

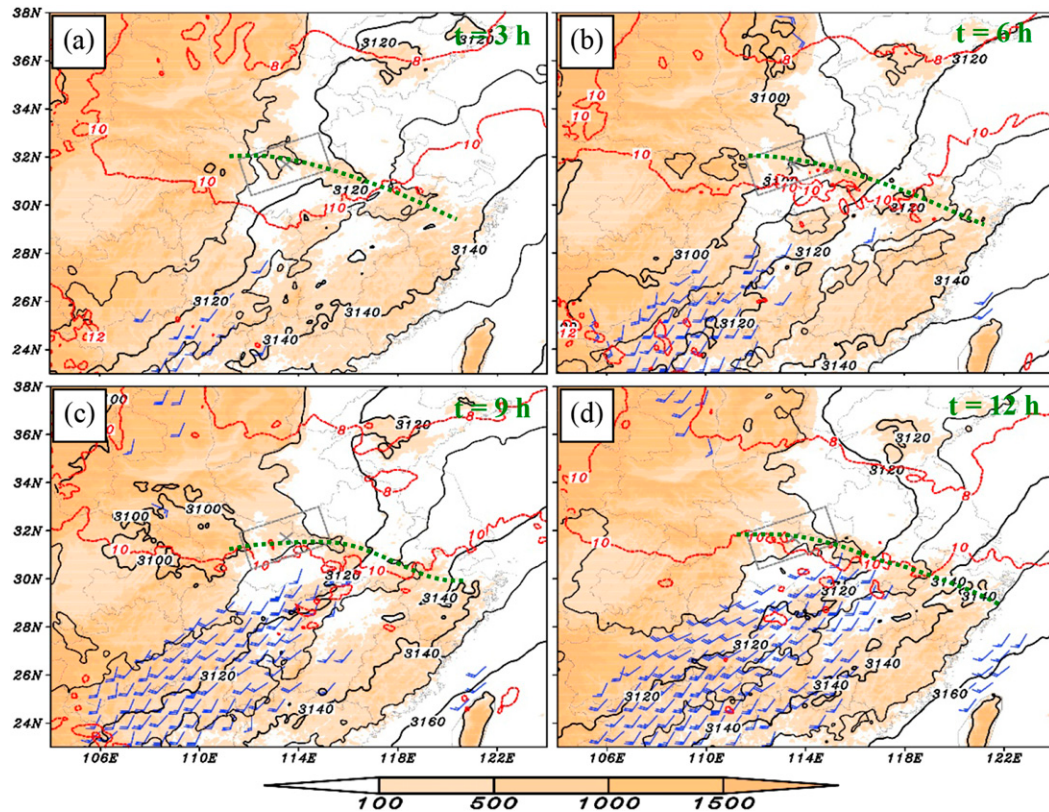


FIG. 6. The 700-hPa geopotential height (black solid lines; gpm) and temperature (red dotted lines; °C), as well as the wind speed $>8 \text{ m s}^{-1}$ at 850 hPa (a full bar represents 5 m s^{-1}) in the ORIG run. The brown shading is the terrain height (m), the gray box shows the key region of the DBV, the gray cross marks the center of the DBV, and the green dashed lines are trough lines.

around the northern boundary of the LLJ, which enhanced convergence in that location.

d. Evolution of kinematic characteristics in the ORIG run

Latent heating dominated the 825–250-hPa layer (not shown), which favored the formation of a DBV by producing positive potential vorticity [this is associated with lower-level cyclonic wind perturbations according to the piecewise potential vorticity inversion (Davis 1992; Fu et al. 2014)], enhancing convection, and causing a decrease in pressure. From $t = 9$ to 12 h, around 112°E , the lower-level northerly wind zone increased and enlarged eastward (Figs. 9c,d), with the zero isotach entering the center of the DBV by $t = 11$ h (this implies DBV formation). During the formation stage, the lower levels around DBM featured intensifying cyclonic vorticity (Figs. 9a–d), strengthening convergence (Figs. 9e–h), and increasing ascending motions. An easterly wind dominated the layer from the surface to ~ 2000 m above (Figs. 9e–h), which mainly represented

the planetary boundary layer, whereas a westerly wind dominated the levels above this layer. The easterly wind zone shrank from $t = 3$ to 12 h (Figs. 9e–h), which was consistent with the lower-level wind reversal process of the mountain–plains solenoid during the same period (Sun and Zhang 2012). This wind reversal process favored the enhancement of lower-level convergence around DBM (the westerly wind perturbation replaced the easterly wind perturbation west of DBM and converged with the remaining easterly wind perturbation around DBM), which also contributed to DBV formation.

4. Mechanisms underlying the formation of the ORIG-run DBV

An area covering the main body of the DBV was determined to be the key region (red dashed box in Fig. 10a). It was used to show the overall features of the DBV. A sensitivity test was applied to this key region; see the smaller blue dashed box and the larger purple dashed box in Fig. 10a, the length and width of which

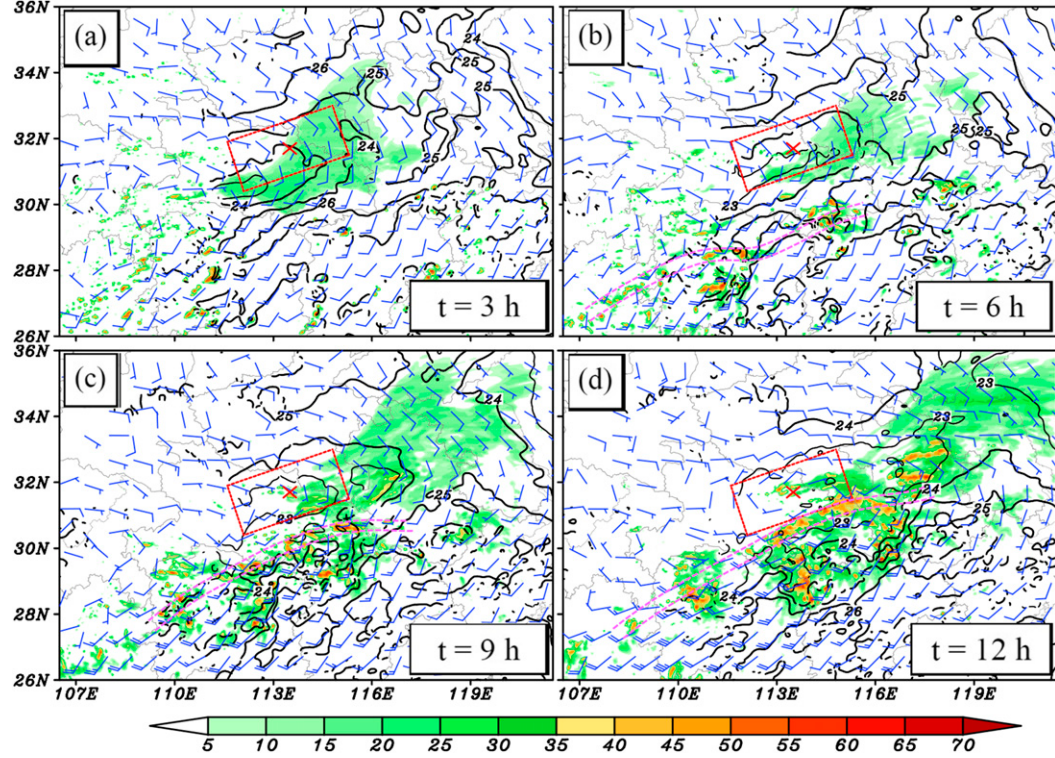


FIG. 7. The composite radar reflectivity (shading; dBZ), the 850-hPa wind field (a full bar represents 5 m s^{-1}), and the 950-hPa temperature (black solid lines; $^{\circ}\text{C}$; $\geq 24^{\circ}\text{C}$ is marked by thick lines and $\leq 23^{\circ}\text{C}$ is represented by thin lines) in the ORIG run. The red box shows the key region of the DBV, the red cross marks the center of the DBV, and the thick purple dashed lines show the main body of the convergent and cyclonic line.

were ~ 10 grid points smaller and ~ 7 grid points larger, respectively, than the key region. Comparisons show the area-averaged vorticity, divergence, vertical velocity, and temperature all had similar variations within the

three boxes (not shown). Moreover, the area-averaged terms of the vorticity budget equation showed the same effects and relative importance within the three boxes (not shown). Therefore, the key region was

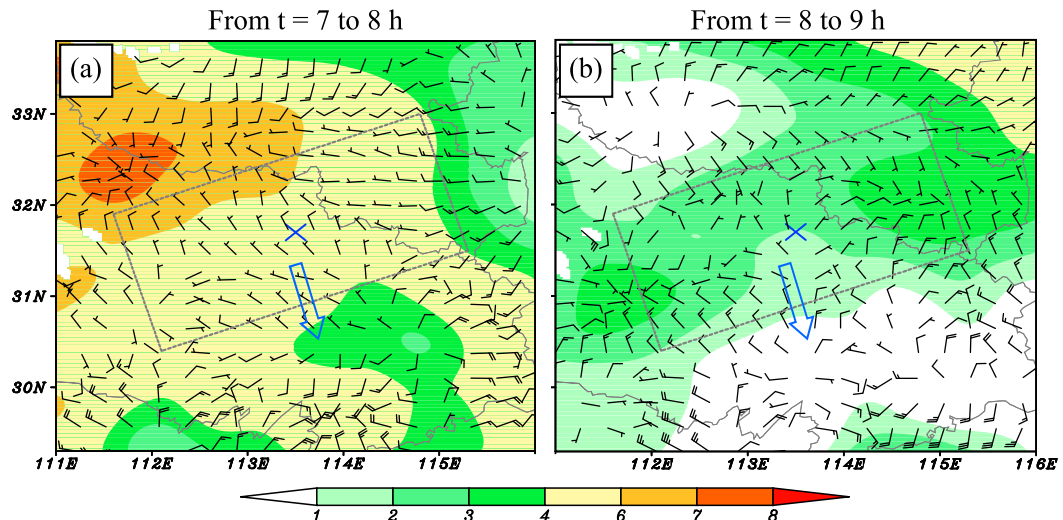


FIG. 8. Hourly variation (the later time minus the earlier time) in the 850-hPa geopotential height (shading; gpm) and the corresponding isallobaric wind (a full bar is 10 m s^{-1}) in the ORIG run. The blue cross marks the center of the DBV, the gray box shows the key region, and the open blue arrow shows the primary direction of the isallobaric wind.

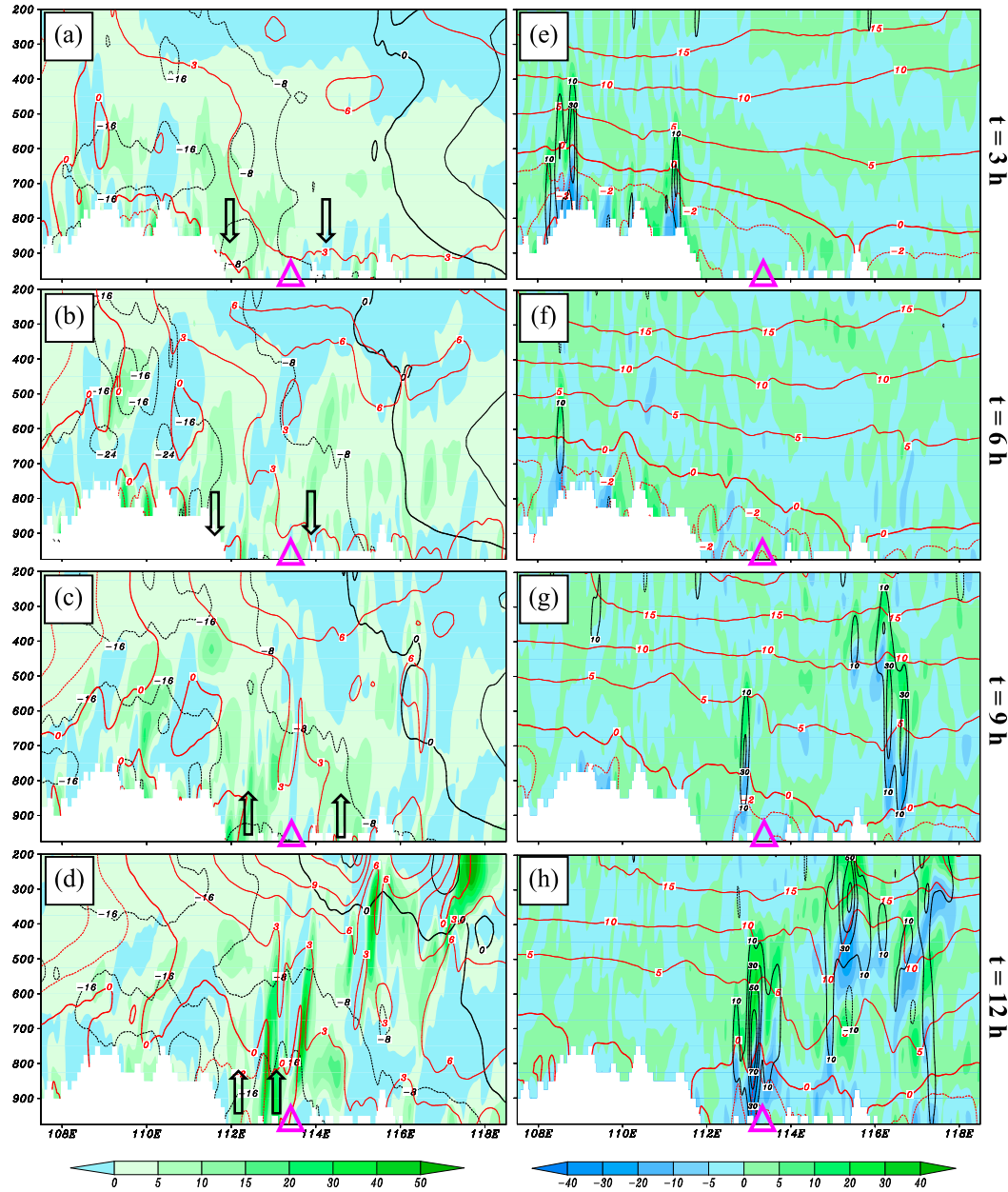


FIG. 9. (a)–(d) Vorticity (shading; 10^{-5} s^{-1}), height deviation relative to the zonal mean in the whole range of d03 (black lines; m), and the meridional wind (red lines; m s^{-1}) along 31.7°N (the central latitude of the center of the DBV) in the ORIG run. (e)–(h) Divergence (shading; 10^{-5} s^{-1}), vertical velocity (black lines; cm s^{-1}), and zonal wind speed (red lines; m s^{-1}) along 31.7°N in the ORIG run. The purple triangles mark the center of the DBV and the black open arrow shows the primary direction of the vertical motion.

insensitive to relatively small changes, which assured its representativeness.

a. Variations of vortex-averaged (key-region averaged) features

The period before the formation of a DBV could be divided into three stages (Fig. 11a). The first stage

occurred before hour 4 (not shown), during which a quasi-stationary shear line intensified gradually around DBM (the key-region-average vorticity increased at a rate of $\sim 0.7 \times 10^{-6} \text{ s}^{-1} \text{ h}^{-1}$). The key region was covered by a stratiform echo and the convective activity was weak (Fig. 7a). The second stage occurred from $t = 5$ to 9 h (Fig. 11a), during which the cyclonic vorticity within

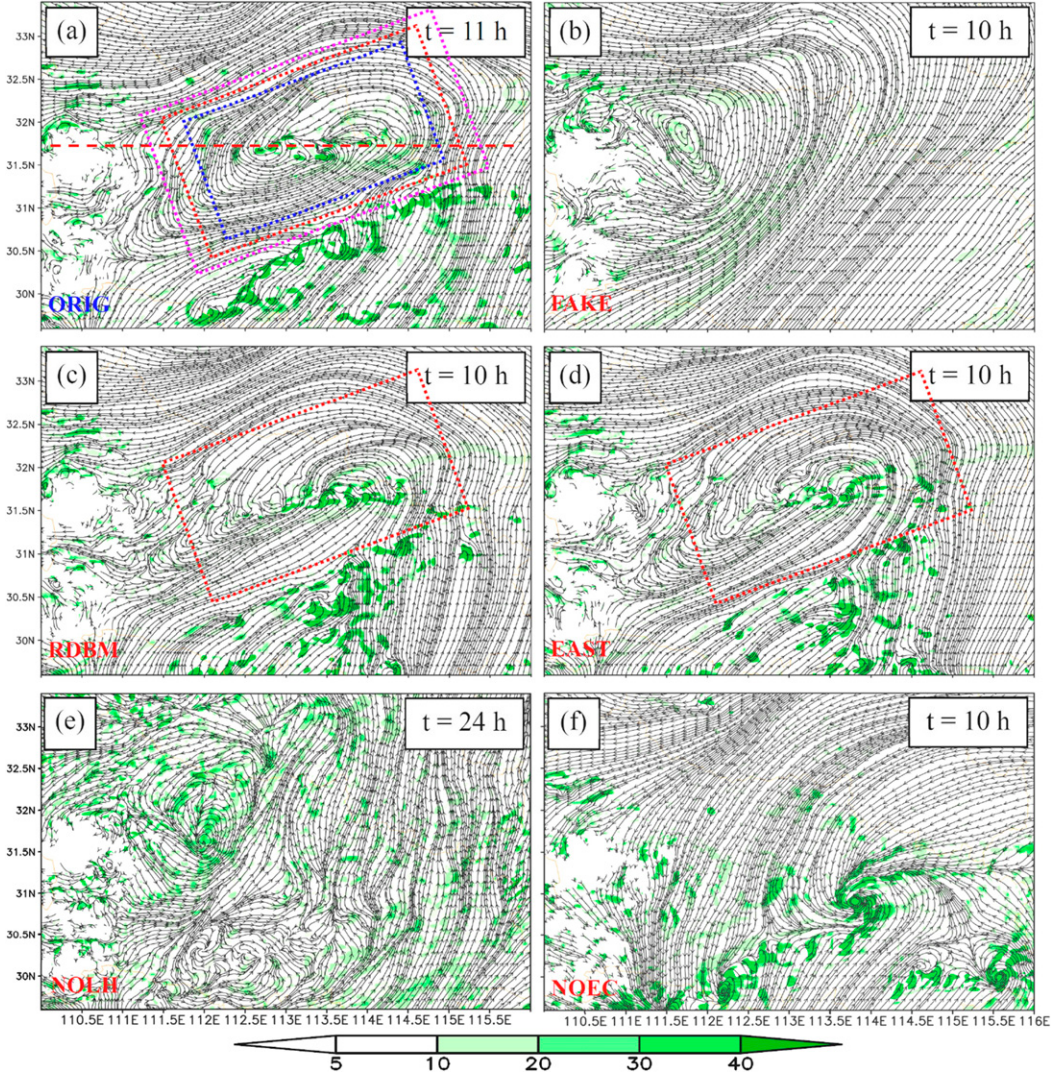


FIG. 10. The 850-hPa streamlines and vorticity (10^{-5} s^{-1}) at the initiation time of the DBV in different semi-idealized experiments (shown at the left-bottom corner of each panel). The dashed rectangles represent the regions for calculating the area average. The red dashed line is the central latitude for cross sections (see Fig. 9).

the key region increased rapidly ($\sim 3.0 \times 10^{-6} \text{ s}^{-1} \text{ h}^{-1}$) and the convective activity also developed quickly (Figs. 7b,c). The rapid growth in cyclonic vorticity mainly corresponded to an enhancement of the lower-level shear line around DBM (Fig. 12). The third stage was from $t = 9$ to 11 h (Fig. 11a), during which the key-region-averaged vorticity remained strong but varied slowly ($\sim 0.3 \times 10^{-6} \text{ s}^{-1} \text{ h}^{-1}$), and the convection was active (Fig. 7d). The DBV formed in the third stage, which was characterized by slow-changing strong cyclonic vorticity. As the solid purple line in Fig. 12 shows, around the key region's western boundary there was a southwest–northeast stretching shear line. At $t = 10 \text{ h}$, a meso- β -scale vortex (labeled “A”) formed and moved northeastward along the shear line (Fig. 12c). Meanwhile, another meso- β -scale vortex (labeled “B”)

formed within the key region and maintained a quasi-stationary position. From $t = 10.5 \text{ h}$ onward, vortex A began to merge with vortex B (Fig. 12d), which enlarged the area of vortex B. By $t = 11 \text{ h}$, vortex A had completely merged into vortex B, which resulted in DBV formation (Fig. 10a). To define the formation of a DBV, two conditions should be satisfied. A significant positive vorticity center ($\geq 10^{-4} \text{ s}^{-1}$) was established from $t = 9 \text{ h}$ onward (not shown), and a meso- α -scale closed vortex center was created after the appearance of a northerly wind around the middle section of the key region's western boundary (Fig. 10a). Thus, the appearance of northerly wind could be regarded as an indicator of the formation of the ORIG-run DBV.

The variations of the key-region-averaged divergence and vertical motions could be divided into two stages,

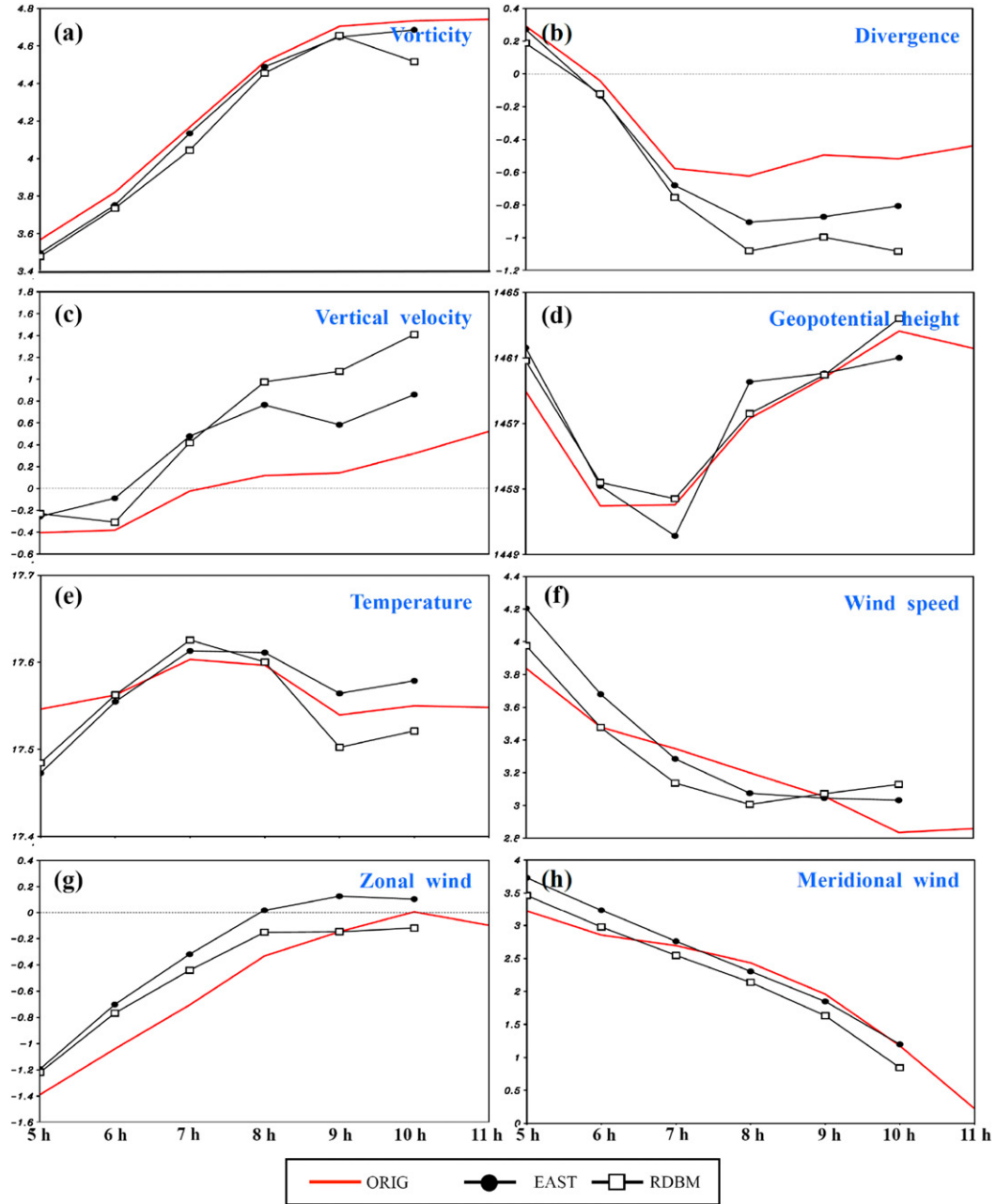


FIG. 11. Key-region-averaged (a) vorticity (10^{-5} s^{-1}), (b) divergence (10^{-5} s^{-1}), (c) vertical velocity (cm s^{-1}), (d) geopotential height (gpm), (e) temperature ($^{\circ}\text{C}$), (f) wind speed (m s^{-1}), (g) zonal wind speed (m s^{-1}), and (h) meridional wind speed (m s^{-1}) at 850 hPa, from the ORIG, EAST, and RDBM experiments.

respectively (Figs. 11b,c): a divergence dominated key region before 5 h (not shown) and then convergence dominated this region from $t = 6 \text{ h}$ onward. In contrast, the transition from descending to ascending motions occurred approximately 1 h later than the transition of divergence. This implies that the lower-level convergence might be an important trigger for the convective activity. As the LLJ enhanced and enlarged northward,

convergence north of the LLJ intensified, moved northward, and entered the key region by $t = 6 \text{ h}$ (Fig. 13f). This caused the condition of the key region to change from divergence to convergence (Fig. 11b). As a result, under abundant moisture conditions (Figs. 13b–d), from $t = 6 \text{ h}$ onward, convection (Figs. 7b–d) and precipitation began to increase significantly around the key region (Figs. 13b–d). Correspondingly, because of the

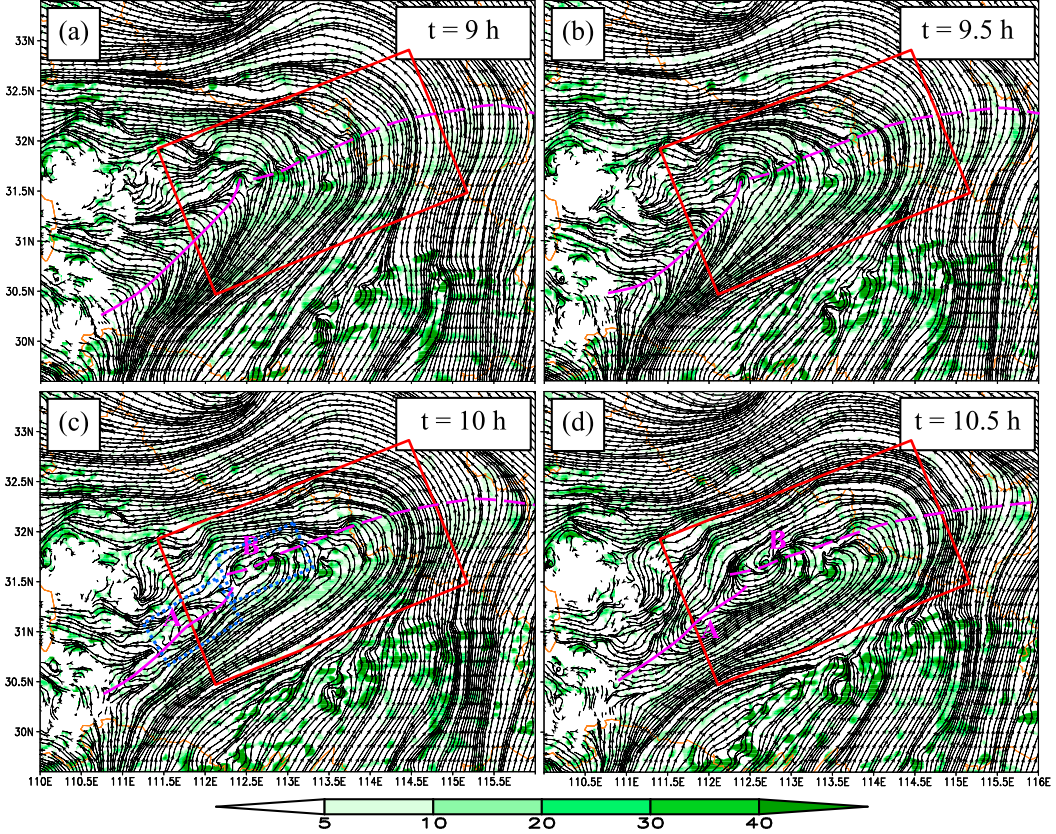


FIG. 12. The 850-hPa streamlines and vorticity (shading; 10^{-5} s^{-1}) in the ORIG run, where the purple solid and dashed lines mark the shear line; labels “A” and “B” mark the small vortices (blue dashed boxes outline their ranges).

evaporative cooling of falling precipitation, the cold pool intensified (Figs. 13f–h), which contributed to lower-level pressure/height rising. However, as Fig. 11d shows, instead of pressure rising, the key-region-averaged geopotential height lowered before $t = 6\text{ h}$. This was because, except for the cold pool-related pressure-rising effects, the key region was also affected by pressure-lowering effects from the warm advection associated with the shortwave trough (Fig. 5b) and transversal trough (Fig. 6), as well as by latent heating. Before $t = 6\text{ h}$, pressure-lowering effects dominated the key region. Then, from $t = 7\text{ h}$ onward, because of the enhancement of the cold pool⁸ (Figs. 13f–h), pressure-rising effects overwhelmed pressure-lowering effects. Thus, the key region mainly featured a rise in height/pressure (Fig. 11d). This triggered a northerly isallobaric wind around the

southern boundary of the key region (Fig. 8), contributing to the intensification of convergence.

Before the formation of a DBV, the key-region-averaged zonal, meridional, and horizontal wind all decreased in intensity (Figs. 11f–h). When a DBV formed ($t = 11\text{ h}$), the key-region-averaged zonal and meridional wind was close to zero. This indicates that the DBV had an approximately central symmetry. Because the steering flow was weak, the DBV would maintain quasi-stationary behavior immediately after formation, which can be confirmed by Figs. 4b and 4c.

b. Vorticity budgets during the formation stage

As Fig. 14 shows, the balance of the vorticity budget equation was good after ignoring friction-related effects. The key region experienced a significant increase in cyclonic vorticity (Fig. 11a), mainly because of the convergence-related STR and VAV. This was consistent with the results of calculations for PL-DBVs reported by Fu et al. (2016). The VAV term, which is determined by the vertical motion and the vertical gradient of vorticity (section 2c) remained positive (Fig. 14), with notable

⁸Because $t = 7\text{ h}$ corresponded to 2100 BST, which was $\sim 1\text{ h}$ after sunset and had no shortwave radiation input, the diurnal cycle of temperature in the lower troposphere also contributed to the cooling within the key region.

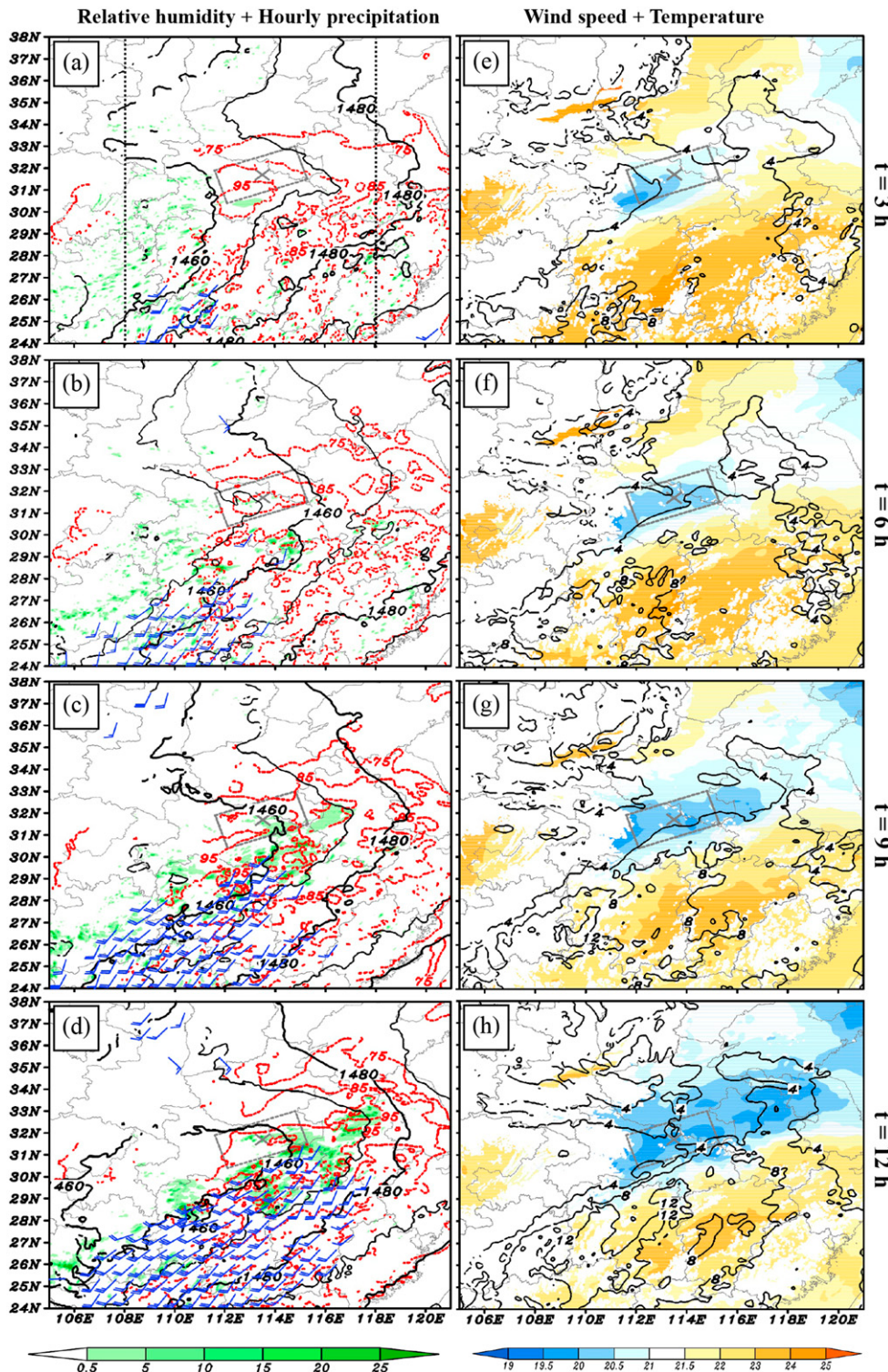


FIG. 13. (a)–(d) Hourly precipitation (shading; mm), lower-level (950–850 hPa) averaged relative humidity (red dashed lines; %), and 850-hPa wind barbs (blue bars; a full bar is 4 m s^{-1}) in the ORIG run. (e)–(h) Lower-level (950–850 hPa) averaged temperature (shading; $^{\circ}\text{C}$), and 850-hPa wind speed (black solid lines; m s^{-1}) in the ORIG run. The gray box marks key region of the DBV, the gray cross marks location of initiation of the ORIG-run DBV, and the thick black dotted lines in (a) show the range for calculating the zonal mean of the lower-level transversal trough (Figs. 19a,b).

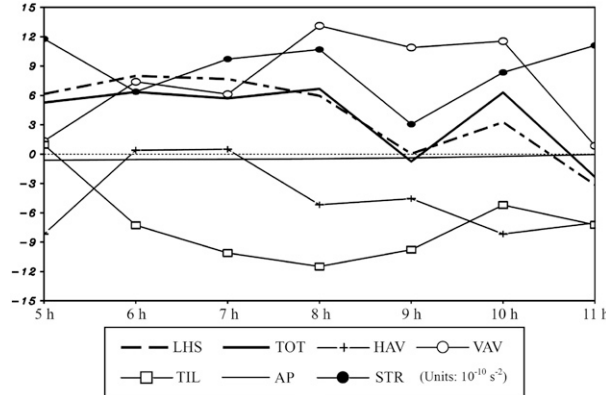


FIG. 14. Key-region-averaged vorticity budget terms at 850 hPa (10^{-10} s^{-2}) in the ORIG run, where LHS is the left-hand-side term (i.e., the time derivative).

changes in the vorticity sources and transport directions. As the red line in Fig. 11c shows, before $t = 7$ h, descending motions dominated the key region. During this period, in the lower troposphere, the cyclonic vorticity above 850 hPa was stronger than that below 850 hPa (not shown). Thus, before $t = 7$ h, the positive VAV was mainly due to the downward transport of a high cyclonic vorticity above 850 hPa. After $t = 7$ h, following the northward enlargement of the LLJ, lower-level convergence was enhanced within the key region (Figs. 9g,h) and ascending motions appeared (Fig. 11c). Strong cyclonic-vorticity cells appeared below 850 hPa, mainly owing to the convergence-related STR in the northern terminus of the LLJ (not shown). During this period, upward motions transported the strong cyclonic vorticity below 850 hPa upward (not shown), which also resulted in a positive VAV.

Before the formation of a DBV, TIL and HAV primarily reduced cyclonic vorticity within the key region (Fig. 14), which was detrimental to the formation of a vortex. The key region served as a source of cyclonic vorticity, exporting cyclonic vorticity ($\text{HAV} < 0$) mainly through its northern boundary, the southern section of its eastern boundary, and the northern section of its western boundary (not shown). The inward transport of cyclonic vorticity also appeared via the southern boundary of the key region. The strong southwest–northeast-oriented cyclonic-vorticity line around the southern boundary of the DBV (Figs. 4a,b) was its main cyclonic-vorticity source. This inward transport partially offset the cyclonic-vorticity loss within the key region.

TIL was weak before $t = 6$ h (Fig. 14) because convective activity around the key region was inactive (Fig. 7a). From $t = 6$ h onward, convection around the

southern boundary of the key region intensified rapidly (Figs. 7b–d). As a result, TIL increased significantly (Fig. 14). Time-averaged (from $t = 6$ to 11 h when TIL was strong) horizontal vorticity and ascending motions were used to show how tilting affected the variation of vorticity (Fig. 15). The key region was further divided evenly into four parts, within which horizontal vorticity was averaged. As Figs. 15a and 15b show, the horizontal vorticity vector mainly pointed northwestward, with the y -direction component (hv_y) stronger than the x -direction component (hv_x). This was consistent with the vertical wind shear of the key region (Fig. 15d). The intensity of hv_x increased to the west (boxes 1 and 3 had a stronger hv_x), while the intensity of hv_y decreased to the north (hv_y was stronger in boxes 3 and 4). Boxes with stronger horizontal vorticity (i.e., boxes 1, 3, and 4) were analyzed. For the westward-pointing hv_x (Fig. 15a), the zonal distribution of vertical motions determined the effect of tilting. As Fig. 15c shows, ascending motions within box 6 (which equals box 1 plus box 3) were weaker than those in boxes 1 and 3. Therefore, hv_x within boxes 1 and 3 was lifted relative to box 6, which resulted in anticyclonic vorticity within boxes 1 and 3. For the northward pointing hv_y (Fig. 15b), the meridional distribution of vertical motions determined the tilting effect. Because box 5 (that equals box 3 plus box 4) had stronger ascending motions than those within boxes 3 and 4 (Fig. 15c), hv_y within boxes 3 and 4 was lowered relative to box 5, which produced anticyclonic vorticity within boxes 3 and 4. These results were confirmed by the averages of TIL within the corresponding boxes.

The meso- β -scale vortices A and B were crucial to the formation of a DBV (Fig. 12). Therefore, a vorticity budget was applied to these vortices, which was averaged in the two blue dashed boxes shown in Fig. 12c. The corresponding results were averaged from $t = 9$ to 10 h (at 30-min intervals) to identify the mechanisms underlying their formation. As Table 3 details, vortices A and B formed through different mechanisms. For vortex A, tilting, which was closely related to the convective activity dominated cyclonic-vorticity production, whereas stretching was the most detrimental factor. Other factors, including the horizontal and vertical transports of vorticity and the planetary vorticity advection, mainly had a negative effect on the formation of vortex A. For vortex B, the horizontal vorticity transport governed the increase in its cyclonic vorticity, and upward vorticity transport was the second most favorable factor. The other parameters (i.e., TIL, AP, and STR) were mainly detrimental to the formation of vortex B, with tilting having the most negative effects. Overall, mechanisms governing the vorticity variation of the meso- β -scale vortices A and B (Table 3) were different from those governing the DBV (Fig. 14).

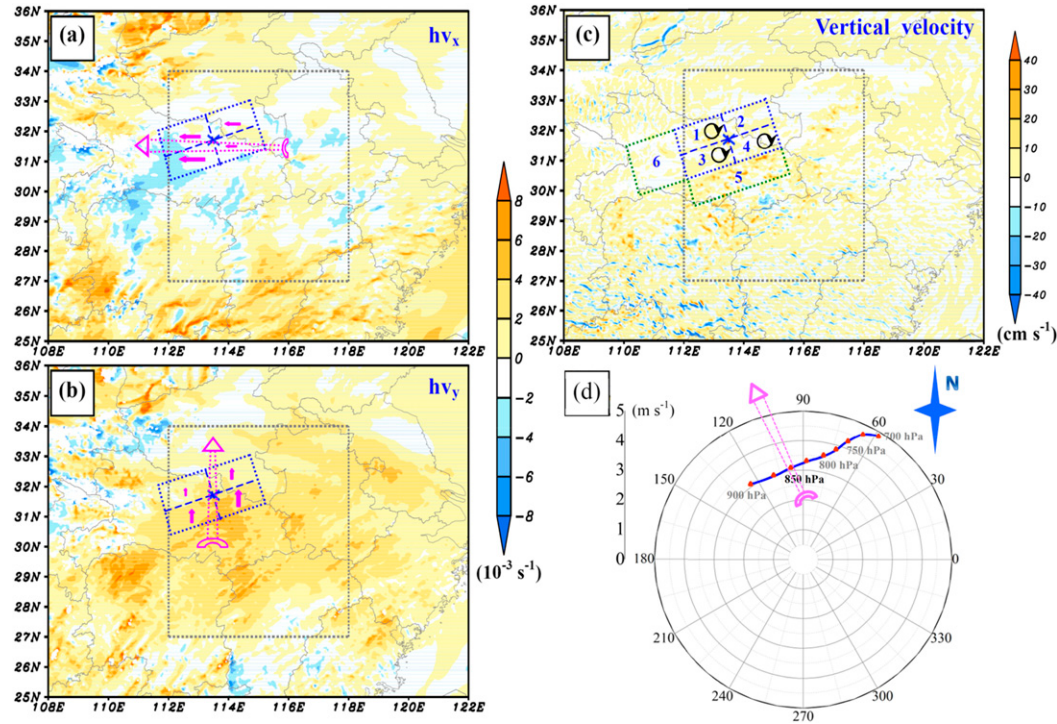


FIG. 15. (a)–(c) Time-averaged ($t = 6\text{--}11\text{ h}$) horizontal vorticity vector and vertical motions at 850 hPa in the ORIG run, where hv_x and hv_y represent the x - and y -direction components, respectively; solid purple arrows show the intensity of the horizontal vorticity (larger size means larger value), open purple dashed arrows show the mean horizontal vorticity around key region (thicker means larger intensity), the numbers 1–6 mark the regions for analysis, the gray dashed box shows the source region of DBVs, and the circles with arrows show the effects of the term TIL. (d) The lower-level (900–700 hPa) key-region-averaged hodograph, where the open purple dashed arrow shows the direction of the corresponding horizontal vorticity vector.

5. Sensitivity experiments

a. Effects of latent heating/cooling

According to the vertical distribution of latent heating/cooling, above 825 hPa, latent heating was dominant, while below 825 hPa, evaporative cooling was dominant (not shown). As the FAKE run (Table 2) showed, owing to the removal of latent heating, in the upper troposphere, the ULJ east of the 200-hPa trough shrank northeastward (cf. Figs. 5a and 16a), implying that the key region was no longer located in the right entrance region of the ULJ. In the middle troposphere, the FAKE-run 500-hPa shortwave trough shrank westward by $\sim 3^\circ$ relative to the ORIG-run trough (cf. Figs. 5b and 16b). This means that the 500-hPa trough-related favorable quasi-geostrophic forcings for the vortex formation also moved westward. Owing to the breakdown of the positive feedback between ascending motions and latent heating (Raymond and Jiang 1990), convection and precipitation weakened remarkably (cf. Figs. 13c and 17a). This resulted in a reduction in evaporative cooling, and thus the cold pool weakened in intensity and shrank in range (cf.

Figs. 13g and 17b). The reduction in convective activity corresponded to a decrease in lower-level convergence (according to continuity). Therefore, the convergence-related production of cyclonic vorticity around the key region weakened in the FAKE run (not shown).

Following the removal of latent heating/cooling, the key region was no longer favorable for DBV formation in the FAKE run. Instead, the FAKE-run vortex formed $\sim 2^\circ$ west of the key region (Figs. 10a,b), which was consistent with the location of the 500-hPa shortwave trough (cf. Figs. 5b and 16b). Compared with the ORIG-run DBV, the FAKE-run vortex had weaker cyclonic vorticity, a smaller horizontal radius (cf. Figs. 10a and 10b), and a

TABLE 3. Time mean of the area-averaged (within the two boxes in Fig. 12c) vorticity budget terms (10^{-10} s^{-2}) of vortex A and vortex B at 850 hPa of the ORIG run during their formation stages ($t = 9\text{--}10\text{ h}$).

	HAV	VAV	TIL	AP	STR	Total
Vortex A	-9	-5	63	0.04	-15	34
Vortex B	110	20	-78	-0.32	-12	40

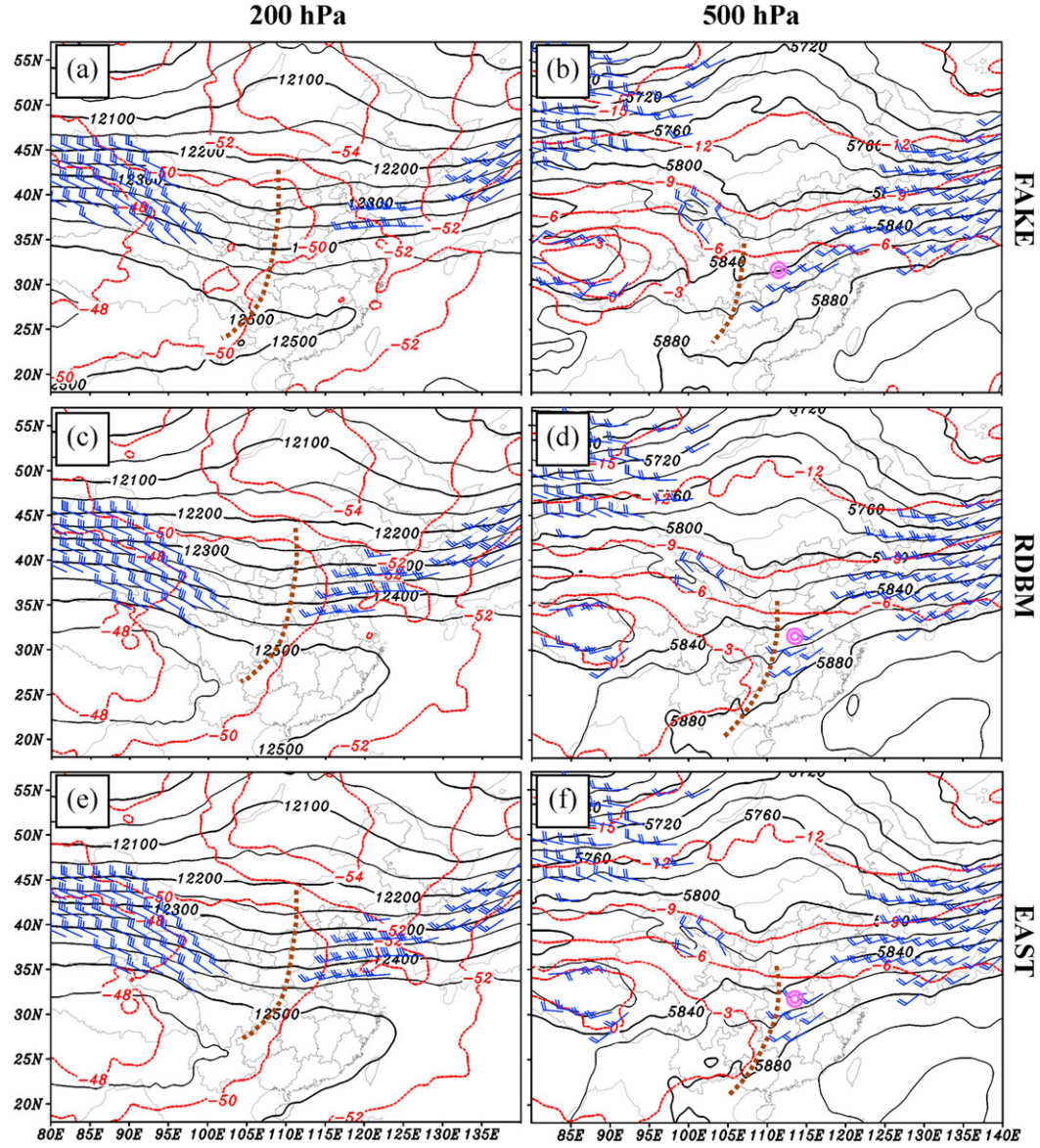


FIG. 16. Geopotential height (black solid lines; gpm), temperature (red dotted lines; °C), and wind speed >25 or 9 m s^{-1} at 200 or 500 hPa (blue wind bar, a full bar represents 10 or 5 m s^{-1} at 200 or 500 hPa, respectively) at $t = 9$ h in the FAKE, RDBM, and EAST runs, where the purple concentric circle shows the center of the corresponding DBV.

much shorter life span (the FAKE-run DBV formed at $t = 10$ h and disappeared at $t = 28$ h). This is consistent with comparisons between the NN (precipitation is light) and PL types (precipitation is heavy) of DBVs documented by Fu et al. (2016). As reported by Raymond and Jiang (1990), certain MCSs achieve longevity as a result of interactions between quasi-balanced vertical motions and the diabatic effects of moist convection. The breakdown of this interaction is a possible reason for the much shorter life span of the FAKE-run DBV. The vorticity budget of this

FAKE-run DBV indicates that the downward transport of cyclonic vorticity was the most favorable factor for its formation (not shown).

The NOLH run (Table 2) was used to investigate the effect of latent heating around/within the DBV. In this run, the cold pool was enhanced, because only evaporative cooling was retained. Neither strong convection nor heavy precipitation appeared around the key region (not shown). Convergence around the southern boundary of the key region weakened remarkably because the LLJ in the NOLH run did not extend as far north as the

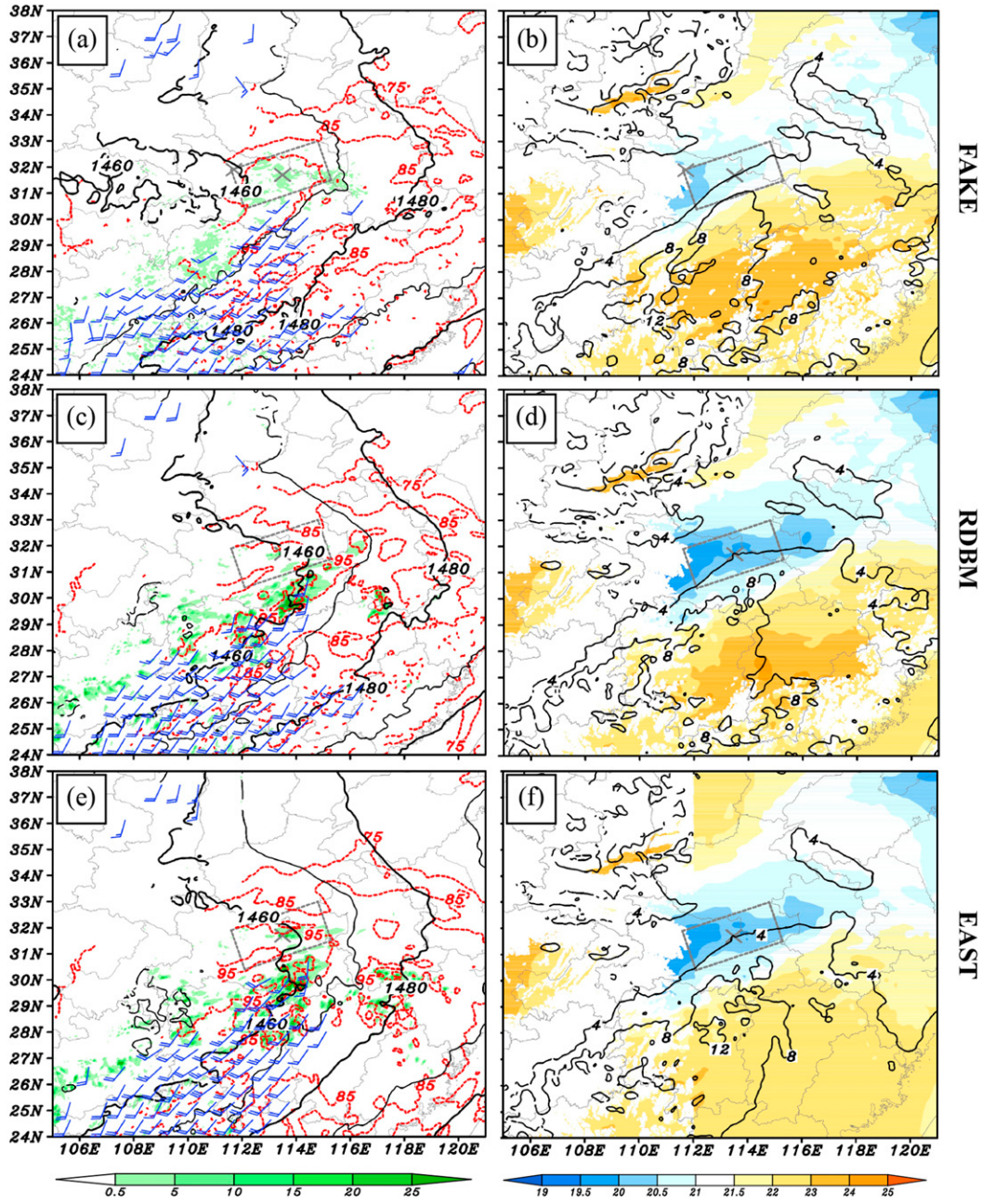


FIG. 17. As in Fig. 13, but for three sensitivity experiments: (a), (b) FAKE, (c), (d) RDBM, and (e), (f) EAST runs) at $t = 9$ h. In (a) and (b) the center of the FAKE-run vortex is also shown by a gray cross.

LLJ did in the ORIG run (not shown). This also reduced the convective activity in the area south of the key region (not shown). From $t = 0$ to 23 h, no DBV formed because the convergence-related STR and convection-related VAV for generating a DBV weakened significantly in the NOLH run, while the inhibition effect of the cold pool strengthened. At $t = 24$ h, a NOLH-run DBV formed (Fig. 10e), mainly as a result of the downward transport of cyclonic vorticity (similar to the

FAKE-run DBV). This vortex lasted for ~ 11 h and dissipated at $t = 35$ h. This confirms the result of the FAKE run—that is, latent heating is not a necessary condition for the formation of a DBV but is critical for prolonging its longevity. The similar results for the FAKE and NOLH runs also indicate that, without latent heating, the DBV has much lighter precipitation and a much smaller radius (cf. Figs. 10a and 10e) than that of the ORIG-run DBV.

The NOEC run ([Table 2](#)) was used to investigate the effect of evaporative cooling around/within the DBV. In contrast to the NOLH run, in the NOEC run, the cold pool almost disappeared, while convection, precipitation, and convergence were enhanced significantly (not shown). All these changes were conducive to trigger a vortex, and at $t = 10$ h a DBV formed ([Fig. 10f](#)) mainly through convergence-related STR and convection-related VAV (similar to the ORIG-run DBV).

b. Effects of the topographic features

The RDBM and EAST runs were designed to clarify whether the topographic features were a decisive condition for the formation of this DBV source ([Table 2](#)). Comparisons among [Figs. 5a](#), [16c](#), and [16e](#) indicated that, during the simulation period, the upper-level weather systems were insensitive to the topographic features around DBM and east of 112°E. In the middle troposphere, the 500-hPa shortwave troughs in the ORIG, RDBM, and EAST runs (including location, orientation, intensity, and wind speed) also had no obvious differences (cf. [Figs. 5b](#), [16d](#), and [16f](#)). Therefore, around the key region, favorable upper- and midlevel conditions for the formation of DBVs were maintained after modifying the topography. The most obvious changes in response to topographic modifications appeared in the lower troposphere ([Fig. 18](#)). Removing the topography resulted in obvious changes in precipitation, temperature, relative humidity, and wind fields (cf. [Figs. 13c](#), [13g](#), [17c–f](#), and [18c–h](#)). Topography usually has complex influences on weather systems through its dynamical (e.g., lifting and friction) and thermodynamical (e.g., sensible/latent heat flux) effects ([Wang and Tan 2014](#)). However, during the simulation period, the topographic modifications did not cause significant changes in the location, orientation, or intensity of the lower-level transversal troughs (cf. [Figs. 13c](#), [17c](#), and [17e](#)), implying that the key region still retained favorable conditions for the formation of DBVs. Correspondingly, vortices in the ORIG, RDBM, and EAST runs formed in almost the same location and had a very similar orientation (cf. [Figs. 10a](#), [10c](#), and [10d](#)). Therefore, the key region was also used to calculate the overall features of the vortices in the RDBM and EAST runs. Both the RDBM- and EAST-run DBVs formed at $t = 10$ h—that is, approximately 1 h earlier than the ORIG-run vortex. The key-region-averaged cyclonic vorticity in these three simulations varied with a similar trend and intensity ([Fig. 11a](#)). This means that the DBV strength was insensitive to detailed topographic features. Similarly, there were no obvious changes in the average geopotential height, temperature, and wind in the key region in response to

the topographic modifications ([Figs. 11d–h](#)). In contrast, the key-region-averaged divergence and vertical velocity clearly changed. The removal of the topography around DBM resulted in an increase (decrease) in zonal wind in the western (eastern) part of the key region ([Fig. 18e](#)). This configuration enhanced the RDBM-run convergence within the key region. Moreover, around the middle section of the key region's southern boundary, meridional wind increased, whereas in other parts it mainly weakened ([Fig. 18g](#)), which also contributed to the intensification of convergence. Similar situations also occurred in the EAST run ([Figs. 18f,h](#)), although there was a weaker intensity ([Fig. 11b](#)). Corresponding to the variation in convergence, the key-region-averaged ascending motions also intensified after the topography was removed ([Fig. 11c](#)).

STR and VAV were the determining factors in the formation of the ORIG-run DBV ([Fig. 14](#)). For the RDBM- and EAST-run DBVs, these two terms were also dominant, but they were stronger mainly owing to the increase in convergence and ascending motions ([Figs. 11b,c](#)). The negative effects of HAV and TIL also increased in the RDBM and EAST runs, offsetting the positive effects of STR and VAV, which resulted in the growth rates of cyclonic vorticity in these two simulations being very close to that of the ORIG run ([Fig. 11a](#)).

6. Possible cause of the DBV source conditions

As [section 5a](#) shows, the longitude of a DBV showed a significant response to the location of the 500-hPa shortwave trough. To further confirm this result, a meridional mean of the shortwave trough (within the latitudes shown in [Fig. 5b](#)) is provided in the right column in [Fig. 19](#). It is obvious that the longitude of the DBV center was strongly related to the location of the mean trough line. The changes in the eastward (westward) location of the 500-hPa shortwave trough corresponded to the eastward (westward) location variations of DBVs. Similarly, the latitude of a DBV displayed clear responses to the latitude of the lower-level transversal trough (left column in [Fig. 19](#)). The northward and southward movements of the transversal trough were consistent with the changes in the northward and southward locations of DBVs, respectively. In contrast, the size of the DBV was not obviously related to the location and intensity of the shortwave trough and the transversal trough (middle column in [Fig. 19](#)).

The DBVs tended to form $\sim 13^\circ$ ahead of the trough line of the 500-hPa shortwave trough (right column in [Fig. 19](#)), where quasigeostrophic forcings associated with warm advection and cyclonic-vorticity advection were favorable. The DBVs also tended to form in the

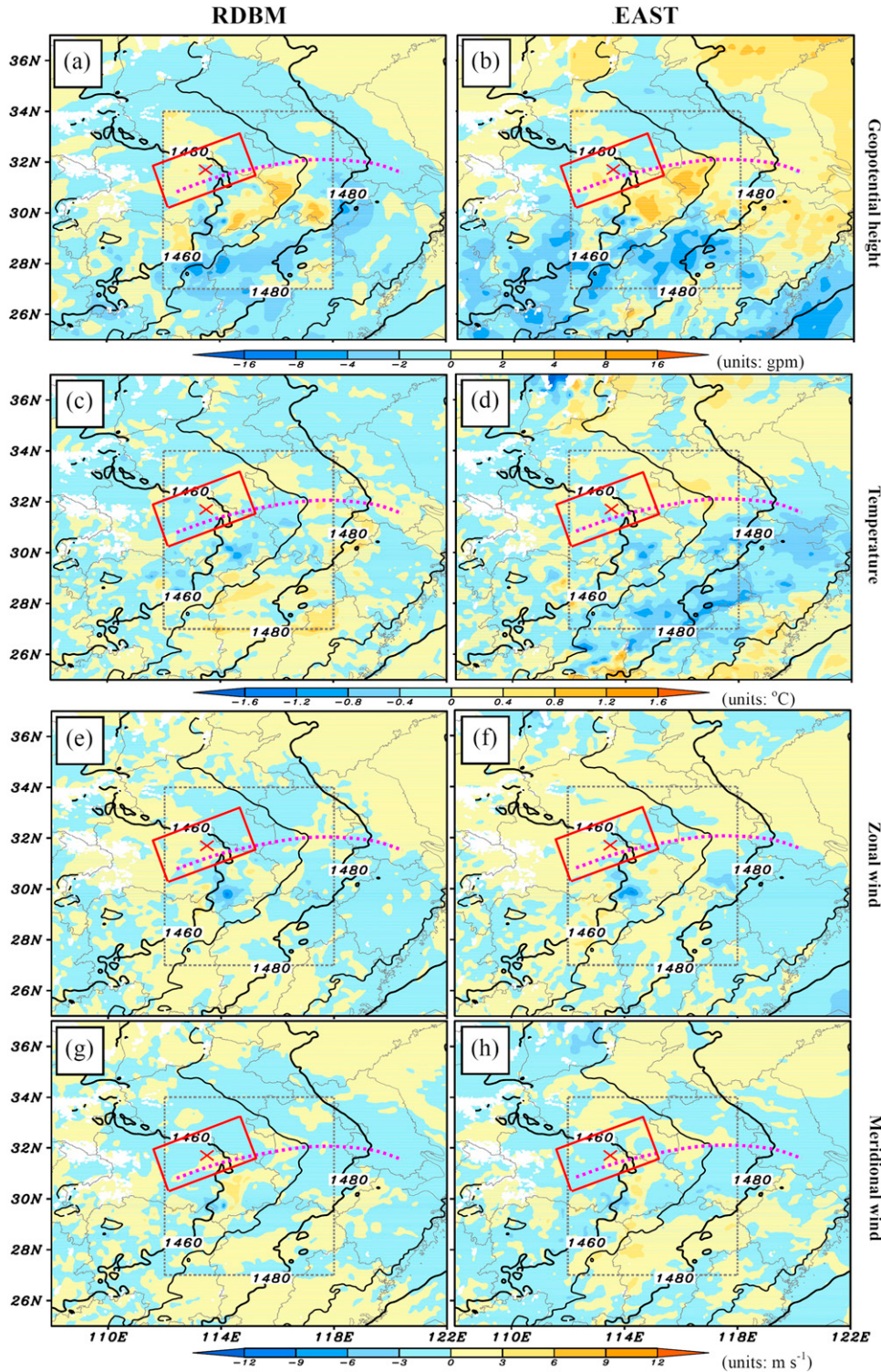


FIG. 18. The 850-hPa differences (shading) (a),(c),(e),(g) between the RDBM run and the ORIG run and (b),(d),(f),(h) between the EAST runs and the ORIG run at $t = 9$ h, where the red cross marks the center of the DBV in the ORIG run, the black solid lines are the 850-hPa geopotential height (gpm) in the ORIG run, and the purple dashed line is its trough line.

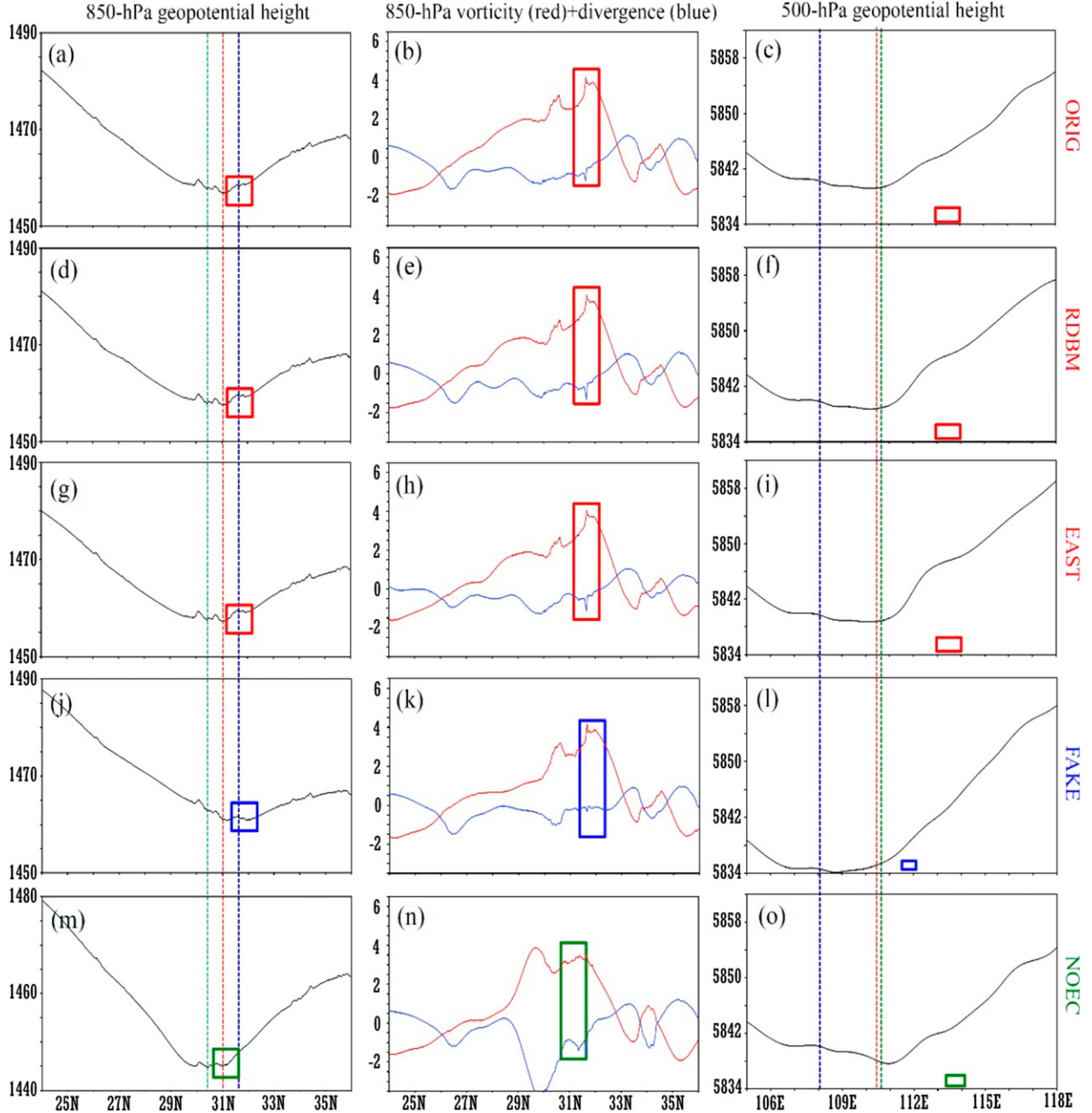


FIG. 19. The time-averaged (from the vortex's formation to 6 h earlier) (left) zonal-mean (in the longitude range shown in Fig. 13a) 850-hPa geopotential height (gpm), (center) zonal-mean 850-hPa vorticity and divergence (10^{-5} s^{-1}), and (right) the meridional-mean (in the latitude range shown in Fig. 5b) 500-hPa geopotential height (gpm). The colors represent ORIG, RDBM, and EAST (red), FAKE (blue), and NOEC (green) runs. In (left), the colored dashed lines are the mean trough lines of the lower-level transversal trough, and the colored rectangles show the location of the DBV's center. In (center), the colored rectangles show the location of the DBV's center. In (right), the colored dashed lines are the mean trough lines of the shortwave trough, and the colored rectangles show the location of the vortex center (bigger size means bigger vortex).

transversal trough's northern section (left column in Fig. 19), where there were cyclonic-vorticity maxima and divergence minima (middle column in Fig. 19). The low pressure/height and high cyclonic vorticity provided a favorable base state for vortex formation.

Similarly, Smith (1984) and Schär (1990) also suggested the importance of a preexisting lower-level shear line in the lee cyclogenesis.

All six semi-idealized simulations (Table 2) showed the superposition of a 500-hPa shortwave trough on the

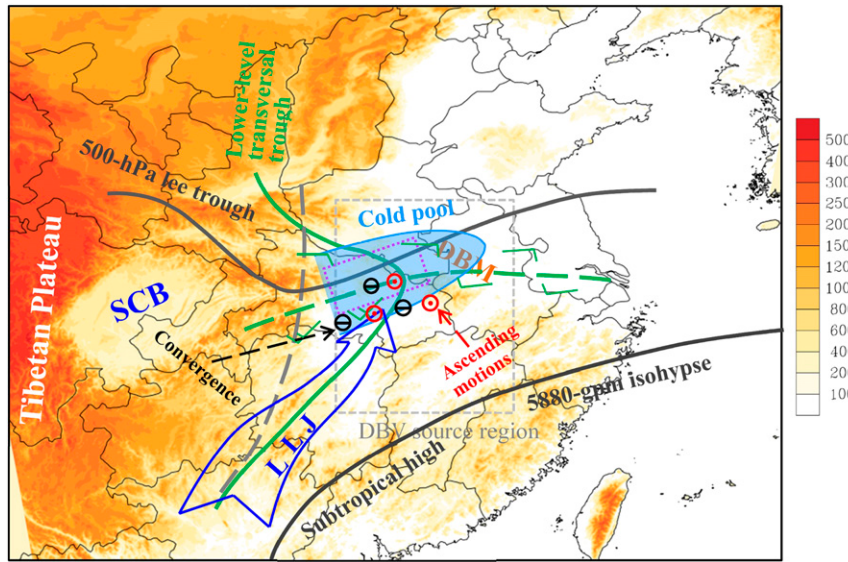


FIG. 20. Schematic illustration of the configuration of the 500-hPa shortwave lee trough and subtropical high (thick gray lines, where the dashed thick gray line represents the trough line), as well as the 850-hPa transversal trough (thick green line, where the dashed thick green line stands for the trough line) and the LLJ (blue arrow). The circle with a horizontal line and the circle with a dot represent the convergence and ascending motions, respectively. The dashed purple box marks the key region of DBV, and the gray dashed box shows the source region of DBVs.

lee side of the second-step terrain and a lower-level transversal trough was a necessary condition for the formation of DBVs. A composite study of 100 DBVs during the formation stage (Zhang et al. 2015) also confirmed this result. In the warm season, the subtropical high over the northwestern Pacific maximizes in intensity and range, with its mean ridge line located around 24°N (Tao 1980; Zhao et al. 2004). A lower-level high/ridge appears repeatedly northeast of the Sichuan basin ($\sim 35^{\circ}\text{N}$) (Tao 1980), mainly owing to the lower-level anticyclonic vorticity produced by the friction around the northern edge of the Tibetan Plateau (Cheng 1986; Chi 1965). A lower-level transversal trough frequently appears between the subtropical high and lower-level high/ridge, with its trough line swinging around DBM (Cheng 1986; Tao 1980; Zhang et al. 2015; Zhao et al. 2004). This provides favorable conditions for the formation of a vortex around DBM. As a type of lee trough, a 500-hPa shortwave trough frequently forms through interactions between the atmosphere and the thermodynamic/dynamic effects of the Tibetan Plateau (Duan and Wu 2005; Ye 1952). After formation, the lee trough moves eastward and superposes the lower-level transversal trough downstream. Because this superposition frequently appears around DBM, the source conditions of the DBVs occur in this region. Therefore, the DBV source conditions are mainly determined by

interactions between the large-scale environmental conditions and the effects of the Tibetan Plateau, rather than the specific topographic features around DBM.

7. Conclusions and discussion

In this study, using semi-idealized simulations based on a composite of 11 long-lived torrential-precipitation-producing PL-DBVs, a schematic model of the formation of a DBV was derived. As Fig. 20 shows, the formation of a DBV is the result of various factors, including quasigeostrophic forcings associated with the 500-hPa shortwave trough, a favorable base state (low pressure and high cyclonic vorticity) related to the lower-level transversal trough, and the accelerating effect of the nocturnal LLJ (transporting moisture, enhancing convergence, triggering or ensuring the persistence of convective activity, and producing cyclonic vorticity). An additional calculation of the quasigeostrophic omega equation (Holton 2004; Rantanen et al. 2017) confirmed that, around the DBM, the quasigeostrophic forcing mechanisms mainly contributed to ascending motions (not shown), but they were not the primary cause of the intense ascending motions in this region. Overall, the ascending motion induced by the temperature advection was stronger than that induced by the vorticity advection. The vorticity budget indicated that convergence-related

(horizontal) shrinking and convection-related vertical transport dominated the increase in cyclonic vorticity associated with the DBV, whereas the tilting effect and outward cyclonic-vorticity transport acted in the opposite manner. Except for the intensity of cyclonic vorticity, its redistribution through transport was also vital for the formation of a DBV. The merging of two meso- β -scale vortices due to TIL and HAV+VAV, respectively, was the key feature in the redistribution of vorticity, and directly resulted in the formation of a DBV.

A possible cause of the formation of the DBV source conditions was provided by this study: the 500-hPa lee shortwave trough and the lower-level transversal trough were the dominant factors in determining the location of the conditions leading to formation of DBVs. When they appeared in the same period, a DBV was likely to be generated. Because these two weather systems frequently occur in regions around the DBM during the warm season (Cheng 1986; Tao 1980; Zhao et al. 2004), the region around DBM becomes a vortex source. Therefore, the formation of the vortex source conditions is mainly due to interactions between the large-scale environmental conditions and the effects of the Tibetan Plateau. In contrast, the formation of the SWV source conditions around the Sichuan basin is significantly different to those of the DBV, because many SWVs form in the absence of a 500-hPa lee trough and without a lower-level transversal trough (Lu 1986; Zhang et al. 2015). The topographic features of the Tibetan Plateau are likely to be the decisive factors in SWV formation (by producing topographically induced vorticity streams) (Wang and Tan 2014).

During the 36-h simulation period, weather systems in the upper and middle troposphere were insensitive to the underlying topographic features around DBM. Although the removal of topography enhanced lower-level convergence and convection around DBM, the lower-level transversal trough did not display any obvious variations in location and orientation. This may explain why the location and orientation of DBVs changed little after removing the topography. Moreover, because of the offset among vorticity budget terms, the growth rate of vortex-averaged cyclonic vorticity changed little, implying that the intensity of a DBV was also insensitive to topographic features. Therefore, the detailed topographic features around DBM were not a decisive condition for DBV formation during the simulation period.

Under favorable conditions, a dry process can also produce a DBV (Figs. 10b,e). Compared with the ORIG-run DBV, the FAKE- and NOLH-run vortices had much weaker intensities, smaller horizontal radii, and much shorter life spans. These results were consistent with the results reported by Fu et al. (2016).

Although latent heating was not a necessary condition for the formation of a DBV, it was critical for prolonging its longevity. The vorticity budget indicated that downward vorticity transport dominated the increase of cyclonic vorticity associated with the vortices in the FAKE and NOLH runs. This was similar to the results of the ORIG-run DBV before $t = 7$ h, when the convective activity was weak.

Similar to MCVs, DBVs are also located in the middle and lower troposphere, but they have larger radii and longer lifespans (James and Johnson 2010a,b; Fu et al. 2016). Synoptic-scale conditions in the middle and lower troposphere during the formation stage of a DBV are similar to those in the initial stage of mesoscale convective complexes (MCCs) (Cotton et al. 1989; Maddox 1983), and are characterized by a midlevel shortwave trough and an LLJ, respectively. However, in the upper troposphere, the DBV is located at the right entrance region of the ULJ, whereas the composite result of Maddox (1983) confirmed that the MCC was located in the right exit region. MCVs tend to form within the stratiform region and result from intense convective activity (Davis and Galarneau 2009; Davis and Trier 2007), whereas the simulated DBVs in this study formed outside the stratiform region. The FAKE and NOLH runs further confirmed that DBVs can form even without any convective activity. Similar to the vorticity budget results of many MCVs, vertical vorticity transport (Kirk 2003; Knievel and Johnson 2003) and convergence (Davis and Galarneau 2009; Olsson and Cotton 1997) are crucial for inducing a DBV. However, tilting, which is vital for triggering some MCVs (Brandles 1990; Zhang 1992), is generally detrimental for the formation of a DBV. This was also confirmed by a composite study of PL-DBVs (Fu et al. 2016). As a type of lee cyclone, the formation of DBVs shares some similarities with other types of lee cyclogenesis (McTaggart-Cowan et al. 2010; Schär 1990; Smith 1984). This includes the favorable quasigeostrophic forcings associated with the lee trough and the advantageous initial condition of a preexisting lower-level shear line. Because DBVs form in the base of the lower-level transversal trough, and no cold or warm fronts appear during the formation stage, its baroclinity and baroclinic energy conversion are generally weaker than typical midlatitude cyclones, which have significant warm and cold fronts (Fu et al. 2013; Holton 2004).

Acknowledgments. The authors thank the National Centers for Environmental Prediction (NCEP) and China Meteorological Administration for providing the data. The authors thank Editor Matthew D. Parker and the four anonymous reviewers for their constructive

suggestions. Sincere thanks are also extended to Profs. Fuqing Zhang and Jimy Dudhia and Dr. Zuowei Xie for their insightful suggestions regarding the sensitivity experiments, model configurations, and calculation of the quasi-geostrophic omega equation. This research was supported by the National Natural Science Foundation of China (41775046, 91637211, 41375053, 41405007, and 91437104).

REFERENCES

- Bartels, D. L., and R. A. Maddox, 1991: Midlevel cyclonic vortices generated by mesoscale convective systems. *Mon. Wea. Rev.*, **119**, 104–118, doi:[10.1175/1520-0493\(1991\)119<0104:MCVGBM>2.0.CO;2](https://doi.org/10.1175/1520-0493(1991)119<0104:MCVGBM>2.0.CO;2).
- Brandes, E. A., 1990: Evolution and structure of the 6–7 May 1985 mesoscale convective system and associated vortex. *Mon. Wea. Rev.*, **118**, 109–127, doi:[10.1175/1520-0493\(1990\)118<0109:EASOTM>2.0.CO;2](https://doi.org/10.1175/1520-0493(1990)118<0109:EASOTM>2.0.CO;2).
- Chen, F., and J. Dudhia, 2001: Coupling an advanced land surface-hydrology model with the Penn State–NCAR MM5 modeling system. Part I: Model implementation and sensitivity. *Mon. Wea. Rev.*, **129**, 569–585, doi:[10.1175/1520-0493\(2001\)129<0569:CAALSH>2.0.CO;2](https://doi.org/10.1175/1520-0493(2001)129<0569:CAALSH>2.0.CO;2).
- Cheng, G.-F., 1986: A study on the formation conditions for heavy rains under troughs and warm shear lines over the middle reaches of Changjiang River in China. *Chin. J. Atmos. Sci.*, **10**, 196–203.
- Chi, L.-R., 1965: Numerical analysis of the process of a low level shear line formation over China. *Acta Meteor. Sin.*, **35**, 1–33.
- Clark, A. J., C. J. Schaffer, W. A. Gallus Jr., and K. Johnson-O’Mara, 2009: Climatology of storm reports relative to upper-level jet streaks. *Wea. Forecasting*, **24**, 1032–1051, doi:[10.1175/2009WAF2222216.1](https://doi.org/10.1175/2009WAF2222216.1).
- , W. A. Gallus, M. Xue, and F.-Y. Kong, 2010: Convective-allowing and convection-parameterizing ensemble forecasts of a mesoscale convective vortex and associated severe weather environment. *Wea. Forecasting*, **25**, 1052–1081, doi:[10.1175/2010WAF2222390.1](https://doi.org/10.1175/2010WAF2222390.1).
- Cotton, W. R., M.-S. Lin, R. L. McAnelly, and C. J. Tremback, 1989: A composite model of mesoscale convective complexes. *Mon. Wea. Rev.*, **117**, 765–783, doi:[10.1175/1520-0493\(1989\)117<0765:ACMOMC>2.0.CO;2](https://doi.org/10.1175/1520-0493(1989)117<0765:ACMOMC>2.0.CO;2).
- Davis, C. A., 1992: Piecewise potential vorticity inversion. *J. Atmos. Sci.*, **49**, 1397–1411, doi:[10.1175/1520-0469\(1992\)049<1397:PPVI>2.0.CO;2](https://doi.org/10.1175/1520-0469(1992)049<1397:PPVI>2.0.CO;2).
- , and S. B. Trier, 2007: Mesoscale convective vortices observed during BAMEX. Part I: Kinematic and thermodynamic structure. *Mon. Wea. Rev.*, **135**, 2029–2049, doi:[10.1175/MWR3398.1](https://doi.org/10.1175/MWR3398.1).
- , and T. J. Galarneau Jr., 2009: The vertical structure of mesoscale convective vortices. *J. Atmos. Sci.*, **66**, 686–704, doi:[10.1175/2008JAS2819.1](https://doi.org/10.1175/2008JAS2819.1).
- , and Coauthors, 2004: The Bow Echo and MCV Experiment: Observations and opportunities. *Bull. Amer. Meteor. Soc.*, **85**, 1075–1093, doi:[10.1175/BAMS-85-8-1075](https://doi.org/10.1175/BAMS-85-8-1075).
- Ding, Y., 1993: *Study on the Lasting Heavy Rainfalls over the Yangtze-Huaihe River Basin in 1991*. China Meteorological Press, 255 pp.
- Duan, A.-M., and G.-X. Wu, 2005: Role of the Tibetan Plateau thermal forcing in the summer climate patterns over subtropical Asia. *Climate Dyn.*, **24**, 793–807, doi:[10.1007/s00382-004-0488-8](https://doi.org/10.1007/s00382-004-0488-8).
- Fu, S.-M., F. Yu, D.-H. Wang, and R.-D. Xia, 2013: A comparison of two kinds of eastward-moving mesoscale vortices during the mei-yu period of 2010. *Sci. China Earth Sci.*, **56**, 282–300, doi:[10.1007/s11430-012-4420-5](https://doi.org/10.1007/s11430-012-4420-5).
- , J.-H. Sun, and J.-R. Sun, 2014: Accelerating two-stage explosive development of an extratropical cyclone over the northwestern Pacific Ocean: A piecewise potential vorticity diagnosis. *Tellus*, **66**, 23210, doi:[10.3402/tellusa.v66.23210](https://doi.org/10.3402/tellusa.v66.23210).
- , W.-L. Li, and J. Ling, 2015a: On the evolution of a long-lived mesoscale vortex over the Yangtze River Basin: Geometric features and interactions among systems of different scales. *J. Geophys. Res. Atmos.*, **120**, 11 889–11 917, doi:[10.1002/2015jd023700](https://doi.org/10.1002/2015jd023700).
- , —, J.-H. Sun, J.-P. Zhang, and Y.-C. Zhang, 2015b: Universal evolution mechanisms and energy conversion characteristics of long-lived mesoscale vortices over the Sichuan Basin. *Atmos. Sci. Lett.*, **16**, 127–134, doi:[10.1002/asl2.533](https://doi.org/10.1002/asl2.533).
- , J.-P. Zhang, J.-H. Sun, and T.-B. Zhao, 2016: Composite analysis of long-lived mesoscale vortices over the middle reaches of the Yangtze River valley: Octant features and evolution mechanisms. *J. Climate*, **29**, 761–781, doi:[10.1175/JCLI-D-15-0175.1](https://doi.org/10.1175/JCLI-D-15-0175.1).
- Galarneau, T. J., L. F. Bosart, C. A. Davis, and R. McTaggart-Cowan, 2009: Baroclinic transition of a long-lived mesoscale convective vortex. *Mon. Wea. Rev.*, **137**, 562–584, doi:[10.1175/2008MWR2651.1](https://doi.org/10.1175/2008MWR2651.1).
- Gao, K., and Y.-M. Xu, 2001: A simulation study of structure of mesovortices along Meiyu front during 22–30 June 1999 (in Chinese). *Chin. J. Atmos. Sci.*, **25**, 740–756.
- He, M.-Y., H.-B. Liu, B. Wang, and D.-L. Zhang, 2016: A modeling study of a low-level jet along the Yun-Gui Plateau in south China. *J. Appl. Meteor. Climatol.*, **55**, 41–60, doi:[10.1175/JAMC-D-15-0067.1](https://doi.org/10.1175/JAMC-D-15-0067.1).
- Holton, J. R., 2004: *An Introduction to Dynamic Meteorology*. 4th ed. Academic Press, 552 pp.
- Hong, S.-Y., and J.-O. Lim, 2006: The WRF single-moment micro-physics scheme (WSM6). *J. Korean Meteor. Soc.*, **42**, 129–151.
- Hu, B.-W., and E.-F. Pan, 1996: Two kinds of cyclonic disturbances and their accompanied heavy rain in the Yangtze River Valley during the Meiyu period (in Chinese). *Quart. J. Appl. Meteor.*, **7**, 138–144.
- James, E. P., and R. H. Johnson, 2010a: Patterns of precipitation and mesolow evolution in midlatitude mesoscale convective vortices. *Mon. Wea. Rev.*, **138**, 909–931, doi:[10.1175/2009MWR3076.1](https://doi.org/10.1175/2009MWR3076.1).
- , and —, 2010b: A climatology of midlatitude mesoscale convective vortices in the Rapid Update Cycle. *Mon. Wea. Rev.*, **138**, 1940–1956, doi:[10.1175/2009MWR3208.1](https://doi.org/10.1175/2009MWR3208.1).
- Kain, J. S., 2004: The Kain–Fritsch convective parameterization: An update. *J. Appl. Meteor.*, **43**, 170–181, doi:[10.1175/1520-0450\(2004\)043<0170:TKCPAU>2.0.CO;2](https://doi.org/10.1175/1520-0450(2004)043<0170:TKCPAU>2.0.CO;2).
- Kirk, J. R., 2003: Comparing the dynamical development of two mesoscale convective vortices. *Mon. Wea. Rev.*, **131**, 862–890, doi:[10.1175/1520-0493\(2003\)131<0862:CTDDOT>2.0.CO;2](https://doi.org/10.1175/1520-0493(2003)131<0862:CTDDOT>2.0.CO;2).
- Knievel, J. C., and R. H. Johnson, 2003: A scale-discriminating vorticity budget for a mesoscale vortex in a midlatitude, continental mesoscale convective system. *J. Atmos. Sci.*, **60**, 781–794, doi:[10.1175/1520-0469\(2003\)060<0781:ASDVBF>2.0.CO;2](https://doi.org/10.1175/1520-0469(2003)060<0781:ASDVBF>2.0.CO;2).
- Lu, J.-H., 1986: *Generality of the Southwest Vortex* (in Chinese). China Meteorological Press, 270 pp.
- Maddox, R. A., 1983: Large-scale meteorological conditions associated with midlatitude, mesoscale convective complexes. *Mon. Wea. Rev.*, **111**, 1475–1493, doi:[10.1175/1520-0493\(1983\)111<1475:LSMCAW>2.0.CO;2](https://doi.org/10.1175/1520-0493(1983)111<1475:LSMCAW>2.0.CO;2).
- Markowski, P., and Y. Richardson, 2010: *Mesoscale Meteorology in Midlatitudes*. Wiley-Blackwell, 407 pp.

- McTaggart-Cowan, R., T. J. Galarneau Jr., L. F. Bosart, and J. A. Milbrandt, 2010: Development and tropical transition of an alpine lee cyclone. Part I: Case analysis and evaluation of numerical guidance. *Mon. Wea. Rev.*, **138**, 2281–2307, doi:[10.1175/2009MWR3147.1](https://doi.org/10.1175/2009MWR3147.1).
- Noh, Y., W. G. Cheon, and S. Raasch, 2001: The improvement of the K-profile model for the PBL using LES. Preprints, *Int. Workshop of Next Generation NWP Model*, Seoul, South Korea, Laboratory for Atmospheric Modeling Research, 65–66.
- Olsson, P. Q., and W. R. Cotton, 1997: Balanced and unbalanced circulations in a primitive equation simulation of a midlatitude MCC. Part II: Analysis of balance. *J. Atmos. Sci.*, **54**, 479–497, doi:[10.1175/1520-0469\(1997\)054<0479:BAUCIA>2.0.CO;2](https://doi.org/10.1175/1520-0469(1997)054<0479:BAUCIA>2.0.CO;2).
- Orlanski, I., 1975: A rational subdivision of scales for atmospheric processes. *Bull. Amer. Meteor. Soc.*, **56**, 527–530.
- Ralph, F. M., L. Armi, J. M. Bane, C. Dorman, W. D. Neff, P. J. Neiman, W. Nuss, and P. O. G. Persson, 1998: Observations and analysis of the 10–11 June 1994 coastally trapped disturbance. *Mon. Wea. Rev.*, **126**, 2435–2465, doi:[10.1175/1520-0493\(1998\)126<2435:OAAOTJ>2.0.CO;2](https://doi.org/10.1175/1520-0493(1998)126<2435:OAAOTJ>2.0.CO;2).
- Rantanen, M., J. Raisanen, J. Lento, O. Stepnyuk, O. Raty, V. Sinclair, and H. Jarvinen, 2017: OZO v.1.0: Software for solving a generalised omega equation and the Zwack–Okossi height tendency equation using WRF model output. *Geosci. Model Dev.*, **10**, 827–841, doi:[10.5194/gmd-10-827-2017](https://doi.org/10.5194/gmd-10-827-2017).
- Raymond, D. J., and H. Jiang, 1990: A theory for long-lived mesoscale convective systems. *J. Atmos. Sci.*, **47**, 3067–3077, doi:[10.1175/1520-0469\(1990\)047<3067:ATFLLM>2.0.CO;2](https://doi.org/10.1175/1520-0469(1990)047<3067:ATFLLM>2.0.CO;2).
- Rose, S. F., P. V. Hobbs, J. D. Locatelli, and M. T. Stoeplinga, 2004: A 10-yr climatology relating the locations of reported tornadoes to the quadrants of upper-level jet streaks. *Wea. Forecasting*, **19**, 301–309, doi:[10.1175/1520-0434\(2004\)019<0301:AYCRTL>2.0.CO;2](https://doi.org/10.1175/1520-0434(2004)019<0301:AYCRTL>2.0.CO;2).
- Saha, S., and Coauthors, 2010: The NCEP Climate Forecast System Reanalysis. *Bull. Amer. Meteor. Soc.*, **91**, 1015–1057, doi:[10.1175/2010BAMS3001.1](https://doi.org/10.1175/2010BAMS3001.1).
- Schär, C., 1990: Quasi-geostrophic lee cyclogenesis. *J. Atmos. Sci.*, **47**, 3044–3066, doi:[10.1175/1520-0469\(1990\)047<3044:QGLC>2.0.CO;2](https://doi.org/10.1175/1520-0469(1990)047<3044:QGLC>2.0.CO;2).
- Schumacher, R. S., 2009: Mechanisms for quasi-stationary behavior in simulated heavy-rain-producing convective systems. *J. Atmos. Sci.*, **66**, 1543–1568, doi:[10.1175/2008JAS2856.1](https://doi.org/10.1175/2008JAS2856.1).
- Skamarock, W. C., and Coauthors, 2008: A description of the Advanced Research WRF version 3. NCAR Tech. Note NCAR/TN-475+STR, 113 pp., doi:[10.5065/D68S4MVH](https://doi.org/10.5065/D68S4MVH).
- Smith, R. B., 1984: A theory of lee cyclogenesis. *J. Atmos. Sci.*, **41**, 1159–1168, doi:[10.1175/1520-0469\(1984\)041<1159:ATOLC>2.0.CO;2](https://doi.org/10.1175/1520-0469(1984)041<1159:ATOLC>2.0.CO;2).
- Sun, J.-H., and F. Zhang, 2012: Impacts of mountain–plains soleil on diurnal variations of rainfalls along the mei-yu front over the east China plains. *Mon. Wea. Rev.*, **140**, 379–397, doi:[10.1175/MWR-D-11-00041.1](https://doi.org/10.1175/MWR-D-11-00041.1).
- , S.-X. Zhao, G.-K. Xu, and Q.-T. Meng, 2010: Study on a mesoscale convective vortex causing heavy rainfall during the mei-yu season in 2003. *Adv. Atmos. Sci.*, **27**, 1193–1209, doi:[10.1007/s00376-009-9156-6](https://doi.org/10.1007/s00376-009-9156-6).
- Tao, S.-Y., 1980: *Rainstorms in China*. Science Press, 225 pp.
- Van de Wiel, B. J., A. Moene, G. Steeneveld, P. Baas, F. Bosveld, and A. Holtslag, 2010: A conceptual view on inertial oscillations and nocturnal low-level jets. *J. Atmos. Sci.*, **67**, 2679–2689, doi:[10.1175/2010JAS3289.1](https://doi.org/10.1175/2010JAS3289.1).
- Wang, Q.-W., and Z.-M. Tan, 2014: Multi-scale topographic control of southwest vortex formation in Tibetan Plateau region in an idealized simulation. *J. Geophys. Res. Atmos.*, **119**, 11 543–11 561, doi:[10.1002/2014JD021898](https://doi.org/10.1002/2014JD021898).
- Wei, W., H. S. Zhang, and X. X. Ye, 2014: Comparison of low-level jets along the north coast of China in summer. *J. Geophys. Res. Atmos.*, **119**, 9692–9706, doi:[10.1002/2014JD021476](https://doi.org/10.1002/2014JD021476).
- Yang, Y.-M., W.-L. Gu, R.-L. Zhao, and J. Liu, 2010: The statistical analysis of low vortex during Meiyu season in the lower reaches of the Yangtze (in Chinese). *J. Appl. Meteor. Sci.*, **21**, 11–18.
- Ye, D.-Z., 1952: Effect of Tibet Plateau on the seasonal change of the atmospheric circulation. *Acta Meteor. Sin.*, **22**, 33–47.
- Zhang, D.-L., 1992: The formation of a cooling-induced mesovortex in the trailing stratiform region of a midlatitude squall line. *Mon. Wea. Rev.*, **120**, 2763–2785, doi:[10.1175/1520-0493\(1992\)120<2763:TFOACI>2.0.CO;2](https://doi.org/10.1175/1520-0493(1992)120<2763:TFOACI>2.0.CO;2).
- Zhang, J.-P., S.-M. Fu, J.-H. Sun, X.-Y. Shen, and Y.-C. Zhang, 2015: A statistical and compositional study on the two types of mesoscale vortices over the Yangtze River basin. *Climatic Environ. Res.*, **20**, 319–336.
- Zhao, S.-X., and Coauthors, 2004: *Study on Mechanism of Formation and Development of Heavy Rainfalls on Meiyu Front in Yangtze River*. China Meteorological Press, 282 pp.
- Zhou, Y.-S., and B. Li, 2010: Structural analyses of vortex causing torrential rain over the Changjiang-Huaihe River basin during 8 and 9 July 2003. *Chin. J. Atmos. Sci.*, **34**, 629–639.